P. Bruschi, D. Invernizzi, M. Massari, M. Lovera
Coordinated Manipulator/Spacecraft Control with Systematic Gain Tuning for Space Robot Operations
Journal of Guidance Control and Dynamics, Vol. 49, N. 2, p. 561-576, 2026 (published online 01/01/2026)
doi:10.2514/1.g008811

Coordinated manipulator/spacecraft control with systematic gain tuning for space robots operations

Pietro Bruschi*, Davide Invernizzi†, Mauro Massari‡, and Marco Lovera§
Politecnico di Milano, 20156 Milan, Italy

This paper presents a modeling and control framework tailored for spacecraft equipped with robotic manipulators, focusing on capture maneuvers and stabilization of uncontrolled target objects. The proposed control strategy combines feedback linearization and a Quasi Time-Optimal (QTO) feedback law for the pre-capture phase, and a Lyapunov-based design for post-capture stabilization, with emphasis on addressing actuator saturation. Control gains are tuned using a H_∞ synthesis approach, accommodating various dynamics including sloshing and actuator dynamics effects. Simulation results demonstrate the effectiveness of the proposed designs in two representative scenarios: servicing a large geostationary platform and a small satellite within a Low Earth Orbit constellation.

I. Introduction

Space missions involving robotic manipulation play a critical role in modern space applications, encompassing tasks such as satellite servicing, assembly, and debris removal. These missions demand the development of control strategies capable of handling complex system. Several research projects have been recently funded, or are currently under development [1–5], while others have already successfully accessed a robotic capture in space [6]. Building on some of the outcomes of the GNC and Robotic Arm Combined Control (GRACC) project, funded by ESA [4, 5, 7], this paper focuses on the development and validation of a modeling and control framework for spacecraft equipped with robotic manipulators, designed to execute capture maneuvers and subsequent stabilization of target objects. Specifically, two distinct and relevant scenarios are addressed. For both of them we are considering the inspection phases and the closing approach as already successfully conducted, focusing only in the reach and capture phase (pre-capture), and the detumbling and stabilization phase (post-capture), leaving out the actual capture, for which different control paradigms and more complex models, inclusive of contact dynamics, are required. The first scenario involves servicing a large geostationary platform: the SSL/1300 satellite bus, characterized by semi-collaborative — namely, capable to operate coarse attitude control — and semi-cooperative interactions*. The second scenario pertains to a servicing mission of

*PhD Student, Department of Aerospace Science and Technology; pietro.bruschi@polimi.it.
†Associate Professor, Department of Aerospace Science and Technology; davide.invernizzi@polimi.it.
‡Associate Professor, Department of Aerospace Science and Technology; mauro.massari@polimi.it.
§Full Professor, Department of Aerospace Science and Technology; marco.lovera@polimi.it
*For such definitions, refer to [4, Table 1].

a small satellite within a large Low Earth Orbit (LEO) constellation, akin to configurations found in platforms like Airbus Arrow or the OneWeb constellation. In both scenarios, the spacecraft undertaking the task, referred to as the chaser platform, engages with a target object, necessitating precise control actions to achieve successful capture and stabilization.

From the modeling and control perspective, space robots are multi-body systems characterized by a high level of complexity due to the kinematic and dynamic coupling between their elements. The motion of a single body, whether it is the base of the spacecraft or one of the manipulator links, is transmitted trough the bodies according to the properties of the kinematic chain. To address this complexity, we apply a recursive method to the system of interconnected rigid bodies leveraging the spatial notation proposed by [8], which provides a compact representation of kinematic and dynamic algorithms. This method models the interconnections in terms of forces and kinematic constraints acting at a single-body level, resulting in a large set of equations which are then efficiently solved by exploiting recurrence relations descending from the tree-like structure of the system.

The design of control laws for spacecraft-robotic systems has been subject of extensive research, as highlighted in the recent surveys on the topic [9–11]. The first ideas were focused on controlling the robotic arm while turning off satellite actuators, as shown by [12]. However, when dealing with attitude pointing requirements (important for communication puroposes), a coordinated control approach of both spacecraft and end-effector actuators becomes essential [13, 14]. The fuel-efficient strategy proposed in [15] uses the thrusters, the reaction wheels, and the arm drives in a coordinated way to limit the use of the thrusters and achieve ideally zero fuel consumption in contact-free maneuvering. Recent development in the design of coordinated controllers address robustness issues by accounting for actuator and sensor dynamics, and other effects, such as fuel sloshing and flexible dynamics [7, 16, 17]. These systems often operate in environments characterized by significant uncertainties, that pose critical challenges to the reliability and safety of the mission. Robust control strategies are essential to mitigate these challenges and ensure system stability under adverse conditions. Recent advances can be found in [18], [19].

The control design framework presented in this work is tailored to address the challenges encountered during the pre-capture and post-capture phase of each scenario, leaving out the contact phase. In the pre-capture phase, the focus lies on maneuvering the chaser platform to approach the target object, a task translated into the problem of tracking desired end-effector pose trajectories. Conversely, the post-capture phase prioritizes the stabilization of the multi-body system in a safe configuration, requiring precise control over the attitude of the chaser platform and the joint angles of the manipulator.

In this study, we narrow our focus to enhancing the control laws for pre-capture and stabilization of both uncontrolled and tumbling objects by a space robot equipped with a redundant manipulator. We acknowledge that developing a comprehensive Guidance Navigation and Control (GNC) system is beyond the scope of this work and when developing the control and guidance functions, we assume that there are navigation functions available that estimate the necessary

quantities. We refer readers to [5] for more details on the complete GNC architecture developed in the GRACC project. Instead, incorporating lessons learned in the aforementioned GRACC project, we refine the control laws for improved performance. Notably, this paper tackles the integration of sloshing dynamics in the modeling and control framework, a critical consideration for missions involving fluid-filled spacecraft. Furthermore, the novel control law designed in this work ensures the closed-loop stability of the system in presence of actuator saturation. Specifically, by limiting the control actions, it is possible to prevent actuator overload in case of large errors, while still guaranteeing high performances in the operating conditions.

With respect to prior work [7], wherein the control design was based on a computed torque control law for free-flying robots, the new design features a novel strategy that combines feedback linearization and a Quasi Time-Optimal (QTO) feedback law [20] for the pre-capture phase. This scheme allows for high trajectory tracking performance while mitigating saturation effects inherent in actuation systems. For the post-capture phase, where uncertainty in the inertial parameters of the target object might be larger, a Lyapunov-based design that ensures stabilization with bounded input — that prevents excessive control actions, while ensuring performances — and without relying on the inertial parameters of the system is proposed. As such, the proposed detumbling control law is intrinsically robust to uncertainty in those parameters.

To tune the controller gains, one of the main challenges in nonlinear control, we leverage the fact that the proposed nonlinear control laws behave as PD controllers for small errors and that there are no constraints on the control gains arising from stability analyses applied to the rigid multi-body system. This enables us to employ an H_∞ synthesis approach for fixed-structure controllers on the linearized closed-loop system [21]. Similarly to previous works [7, 17], gain values are systematically determined through this procedure to ensure local stability while accommodating desired performance levels and considering additional effects beyond the rigid body model, such as sloshing, actuator and sensor dynamics. Robustness to parametric uncertainties is studied on the obtained controller throughout a robust analysis, based on μ-theory. Furthermore, a Monte Carlo study is set up to verify the performance of the controllers in uncertain conditions and a nonlinear simulation model.

Simulation results presented in this paper validate the efficacy of the proposed control framework across the considered scenarios, demonstrating robust performance even in the presence of actuator saturation and sloshing effects.

The remainder of the paper is organized as follows. In Section II the approach used for the development of kinematic and dynamic models of the system is presented, with a particular emphasis on the inclusion of the sloshing phenomenon in the multi-body system. Section III illustrates the design of the control algorithm, while a focus on the synthesis of the controller is described in Section IV. Section V explains the guidance algorithm. Finally, in Section VI, the two scenario under study are detailed and the results of the simulations conducted are shown, while in Section VII the conclusions are drawn.

Notation. $\mathbb{R}^n$ denotes the n-dimensional real coordinate space and $\mathbb{R}^{m\times n}$ the set of $m \times n$ real matrices. Given

$x \in \mathbb{R}^n$, $y \in \mathbb{R}^m$, we denote $(x, y) := [x^\top \; y^\top]^\top$. The i-th vector of the canonical basis in $\mathbb{R}^n$ is denoted as $e_i := [0 \; \cdots \; 0 \; 1 \; 0 \; \cdots]^\top$ (1 in the i-th entry, 0 elsewhere) for $i \in \{1, ..., n\}$ and the identity matrix in $\mathbb{R}^{n\times n}$ is $I_n := [e_1 \cdots e_i \cdots e_n]$. Given vectors $x, y \in \mathbb{R}^n$, the standard inner product is defined as $\langle x, y\rangle := x^\top y$. The Euclidean norm of a vector $x \in \mathbb{R}^n$ is $|x| := \sqrt{\langle x, x\rangle}$. For a matrix $A \in \mathbb{R}^{n\times n}$, we define $\text{skew}(A) := A - A^\top$. The n-dimensional unit sphere is denoted as $\mathbb{S}^n := \{x \in \mathbb{R}^{n+1} : |x| = 1\}$. For $n = 1$ (unit circle), we use the identification $\mathbb{S}^1 \simeq \mathbb{R} \bmod 2\pi$. The set $\text{SO}(3) := \{R \in \mathbb{R}^{3\times3} : R^\top R = I_3, \det(R) = 1\}$ is the 3D Special Orthogonal group. The map $S(\cdot) : \mathbb{R}^3 \to \mathfrak{so}(3) := \{W \in \mathbb{R}^{3\times3} : W = -W^\top\}$ is defined such that given $x, y \in \mathbb{R}^3$ one has $S(x)y = x \times y$. The inverse of S is denoted S^{-1}. Position and attitude of a rigid body may be compactly represented by the 6×6 matrix ${}^iX_j := \begin{bmatrix} {}^iR_j & 0_3 \\ S({}^ir_j)\,{}^iR_j & {}^iR_j \end{bmatrix} := X({}^iR_j, {}^ir_j)$, which can also describe a spatial transformation from frame i to frame j. The frame index is omitted whenever a quantity is expressed with respect to the inertial frame.

II. Modeling of Space Robots

In this section, a general framework for the modeling of the kinematics and dynamics of space robots is provided. The powerful spatial notation proposed in [8] is adopted to compactly describe kinematics and dynamics algorithms. Specifically, a recursive method for solving the kinematic chain is outlined, while, the widely adopted Recursive Newton-Euler Algorithm (RNEA) is combined with the Composite Rigid Body Algorithm (CRBA), following the work in [8], to derive the equations of motion of the multi-body system. Eventually, a novel method for the inclusion of the sloshing phenomenon in the dynamics of the system is proposed, to provide more accurate simulation results and, consequently, a better handling of the phenomenon.

A. Space robots configuration and kinematics

The space robot considered in this work is a multi-body system made by a spacecraft base and a robotic arm (manipulator), composed of several links, connected through $N = 7$ planar revolute joints. The following Cartesian reference frames are used to describe the system configuration:

- The Local-Vertical Local-Horizontal (LVLH) frame, denoted as $\mathcal{F}_I$, is fixed at the Center of Mass (CoM) of the target spacecraft, and considered inertial, due to the different timescale of the orbital and relative dynamics.
- The Target body frame, denoted as $\mathcal{F}_T$, is fixed at the CoM of the target spacecraft, and rotating with it.
- The grasping point frame, indicated with $\mathcal{F}_g$, is attached to the grasping point of the target spacecraft.
- *Link frames*, denoted as $\mathcal{F}_n$, $n = 1, \ldots, N$, represent the frames attached at the CoM of the n-th link, with the particular case of $\mathcal{F}_0$ and $\mathcal{F}_N$ indicating the body frame of the base and the end-effector frame, respectively.
- *Joint frames*, denoted as $\mathcal{F}_{m,n}$, with $m = 0, \ldots, N-1$ and n as above, are used to describe the pose of joint m onto body n.

A graphical representation of the aforementioned reference systems is shown in Figure 1, together with the associated

spatial transformations.

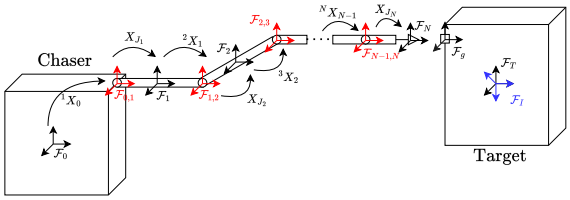

Fig. 1 Geometric model of the space robot.

Given a manipulator with N links connected through revolute joints, the configuration of a space robot is described by elements of the $6 + N$ dimensional manifold

$$\mathcal{M} := \underbrace{\mathbb{R}^3 \times \mathrm{SO}(3)}_{base} \times \underbrace{\mathbb{S}^1 \times \cdots \times \mathbb{S}^1}_{manipulator}, \tag{1}$$

where $\mathbb{S}^1 \times \cdots \times \mathbb{S}^1 =: \mathbb{T}_N$ is the N-dimensional torus. Denoting with $R_0 \in \mathrm{SO}(3)$ the rotation matrix transforming coordinates from $\mathcal{F}_0$ to an inertial reference frame $\mathcal{F}_I$, with $r_0 \in \mathbb{R}^3$ the position vector of the base CoM with respect to $\mathcal{F}_I$ and with $q \in \mathbb{T}^N$ the joint angles of the manipulator, the kinematics of the space robot according to the joint-space formulation can be written as:

$$\dot{R}_0 = R_0 S(\omega_0) \tag{2}$$

$$\dot{r}_0 = R_0 v_0 \tag{3}$$

$$\dot{q} = \omega_q \tag{4}$$

where $\omega_0 \in \mathbb{R}^3$ and $v_0 \in \mathbb{R}^3$ represent the base angular and linear velocity expressed in the body frame, respectively, and $\omega_q \in \mathbb{R}^N$ is the vector of joint angles velocities.

The pose of the end-effector is a crucial quantity for the design of guidance and control algorithms. Such quantity may be retrieved by relying on a forward kinematics algorithm, since it depends upon the manipulator configuration (q) and can be compactly written in product form using spatial transformations as follows:

$$X_N = X_0 \prod_{1}^{N} {}^{i-1}X_i X_{J_i}^{-1}(q_i), \tag{5}$$

where $X_{J_i}^{-1}(q_i) := X({}^iR_{i-1,i}(q_i), {}^ir_{i-1,i})^{-1}$, is the inverse of the joint transformation, representing (without loss of generality) a rotation about the third axis of the joint frame ${}^iR_{i-1,i}(q_i) := \begin{bmatrix} \cos(q_i) & \sin(q_i) & 0 \\ -\sin(q_i) & \cos(q_i) & 0 \\ 0 & 0 & 1 \end{bmatrix}$ combined with a constant

translation ${}^{i}r_{i-1,i}$ (see, again, Figure 1 for a representation of the various transformations involved along the kinematic chain).

B. Dynamics

To describe the dynamics of space robots, the recursive formulation proposed by [8] has been chosen. It is assumed that there exists a clear time-scale separation between the orbital dynamics and the relative dynamics, as one for example in [14–16]. This separation allows us to disregard the influence of orbital effects within the framework of the Clohessy-Wiltshire equations. Consequently, the capture operation can be analyzed under the simplifying assumption that the system behaves as if it were stationary on the ground.

The considered approach enables efficient modeling of complex interconnections between bodies without the need for time-consuming manual derivations. Recursive methods must be preferred over explicit ones [22] whenever computational efficiency is of interest or when deriving equations in closed form is challenging due to complex configurations or a large number of external forces. While in a previous work the recursive method was used to easily include orbital effects into the space robot dynamics, in this work we exploit the method to include sloshing phenomena.

The considered procedure starts from the definition of the equations of motion describing the dynamics of a floating-base robot [8, Chapter 9]:

$$H(q)\begin{bmatrix}\dot{\omega}_0\\ \dot{v}_0\\ \dot{\omega}_q\end{bmatrix} + c\left(\omega_0, v_0, \omega_q, q, f\right) = \begin{bmatrix}\tau_0\\ f_0\\ \tau_q\end{bmatrix} \tag{6}$$

where $\tau_0,\ f_0 \in \mathbb{R}^3$ and $\tau_q \in \mathbb{R}^N$ are base torque, force and joint motor torque, respectively. The joint space inertia matrix is denoted as $H \in \mathbb{R}^{6+N\times 6+N}$ and is computed by means of the CRBA Algorithm [8, Chapter 6]. Vector $c \in \mathbb{R}^{6+N}$ represents the Coriolis/centrifugal term that accounts also for the exogenous term f (this additional term can be used to include the effects of orbital perturbations in the dynamics of the system, as done previously in Pavanello et al.) and can be evaluated using the RNEA algorithm following the procedure outlined in [8, Chapter 5].

Finally, note that the dynamical model used for the pre-capture can be extended to the post-capture phase, with the end-effector inheriting the inertial properties of the target.

C. Sloshing Model Inclusion

The effect of propellant sloshing has been previously accounted for only at gain synthesis time in previous work [4, 5, 7], by considering an equivalent spring mass damper model, which is recognized to be the best model to use

in presence of small maneuvers. However, the outcomes have underlined that the presence of sloshing prevents from reaching reliable robust stability results, due to the high degree of uncertainty introduced. For this reason, a novel approach to incorporate the sloshing behavior directly in the dynamics of the system is proposed in this work, thereby allowing for a more realistic representation of the motion of the space robot in nonlinear simulations and to improve the controller synthesis results.

Specifically, a spherical pendulum equivalent model is adopted, which provides a more complete description of nonlinear rotary sloshing behavior compared to the spring mass damper model [23]. Additionally, the pendulum model should be preferred whenever larger maneuvers are involved, such as in the case of aggressive control actions. The analogy between a spherical pendulum and a spherical joint (made up of two revolute joints) is further exploited [24], such that the fuel inside a spherical tank may be modeled as an additional uncontrolled arm with two degrees of freedom and the entire system as a branched multi-body chain.

The pendulum model is built by defining, for each tank, an equivalent length L_p, equal to the radius of the tank, and an equivalent mass m_p, equal to the propellant mass (see Section VI.A). Indeed, from these parameters, and knowing the location of the tank, the RNEA and the CRBA can be applied, by considering an augmented system. The equations of motion are reformulated as follows:

$$H_{aug}(q, q_p) \begin{bmatrix} \dot{\omega}_0 \\ \dot{v}_0 \\ \dot{\omega}_q \\ \dot{\omega}_p \end{bmatrix} + c_{aug}\left(q, q_p, \omega_0, v_0, \omega_q, \omega_p\right) = \begin{bmatrix} \tau_0 \\ f_0 \\ \tau_q \\ 0 \end{bmatrix} \tag{7}$$

where $H_{aug} \in \mathbb{R}^{(6+N+2N_t)\times(6+N+2N_t)}$ and $c_{aug} \in \mathbb{R}^{(6+N+2N_t)}$ account for the inclusion of the new degrees of freedom given by the sloshing variables $q_p = (q_{t_1}, \cdots q_{t_j}, \cdots, q_{t_{N_t}}) \in \mathbb{R}^{2N_t}$, with j ranging from 1 to N_t, namely the number of tanks present in the system. Indeed, $q_{t_j} =: (\theta_{1_j}, \theta_{2_j})$ represents the uncontrolled degrees of freedom of a single pendulum model associated with a tank.

In addition, a damping contribution has been added to each pendulum model, in the term c_{aug}, to achieve a more realistic representation of the motion of the liquid. Specifically, a term proportional to $\dot{q}_p$ is added to the corresponding coefficient in the c_{aug} term. The damping factor is evaluated following [25] by using the formula $c_p = 8\pi L_p^3 \mu$, where μ is the dynamic viscosity of the propellant.

III. Control law design

This section is devoted to presenting the control strategy devised in this work to address both pre-capture and post-capture phases, for the two scenarios illustrated in the Introduction. For the pre-capture phase, the objective of

getting closer to a grasping point located on the target spacecraft can be translated into the problem of tracking a desired pose of the end-effector. In the post-capture phase, instead, the objective is the stabilization of the whole stack (chaser and target) in a safe configuration. It is worth reminding that, such as in previous works (see, *e.g.*, [7]) we have decided to develop a nonlinear controller to be tested in a simulator with a nonlinear plant, but both of them are linearized about an operating point to perform controller synthesis and leverage a systematic gain tuning routine. In the following, we present in detail the development of the control architecture and of its main blocks, and then show in detail the adopted tuning procedure.

A. Overview of the Control Architecture

A closed-loop architecture, which features a classic two step design in which guidance and control are split, has been developed, as represented in Figure 2. By relying on a guidance-control paradigm, the two loops can be treated as separted, thereby performing the synthesis only on the controller. The controller and the guidance are both designed assuming that state measurements are available for the model (6). Hence, the design of guidance and control laws has been performed not considering the sloshing states in the dynamics of the system, while sloshing dynamics has been considered in the nonlinear simulator and the additional sloshing states are incorporated in the plant linearization for controller synthesis.

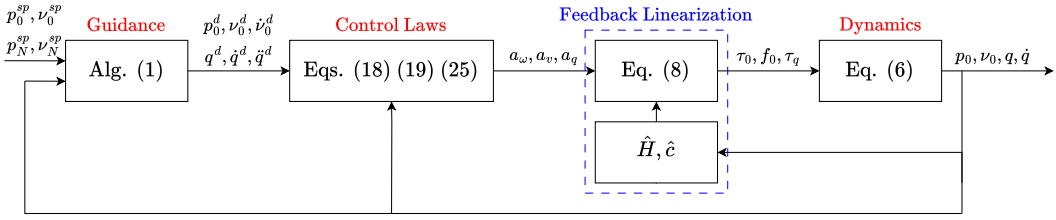

Fig. 2 Closed-loop scheme of the GNC system

The proposed guidance algorithm acts at the kinematic level and converts the high level objectives (depending on the mission phase) into safe desired state trajectory for both the base and the manipulator. In the pre-capture phase, the objective of the guidance is to compute the desired trajectories for the pose of the base and the joint angles to make the base and the end-effector pose asymptotically track desired trajectories. For the post-capture phase, instead, a regulation task must be solved, to ensure that the base attitude is oriented in a suitable fixed direction and joint angles reach a safe constant configuration for the whole stack. As a joint-space architecture has been considered for the development of the control law (state variables include joint angles), the guidance strategy for the pre-capture phase includes an inverse kinematics algorithm which allows converting end-effector pose trajectories to joint angles profiles.

A coordinated controller, namely, one controlling simultaneously both the base pose and manipulator angles using the full model of the system, has been designed to ensure asymptotic tracking of the guidance trajectories. The developed

approach is a novel solution combining feedback linearization and a quasi time-optimal feedback law to achieve high trajectory tracking performance while keeping into account actuation limits.

B. Coordinated control design: pre-capture phase

In the pre-capture phase, the goal of the controller is to ensure asymptotic tracking of the trajectory provided by the guidance function, which is given by a desired pose of the base $p_0^d(t) = \left(r_0^d(t), R_0^d(t)\right)$, joint angles $q^d(t)$ and the corresponding velocities.

To achieve this objective, following a feedback linearizing paradigm, a preliminary input is considered:

$$\begin{bmatrix} \tau_0 \\ f_0 \\ \tau_q \end{bmatrix} = \hat{c}\left(\omega_0, v_0, \omega_q, q\right) + \widehat{H}(q) \begin{bmatrix} a_\omega \\ a_v \\ a_q \end{bmatrix} \tag{8}$$

where $\widehat{H}$ and $\hat{c}$ are, respectively, an estimate of the mass matrix and the Coriolis/centrifugal term, while a_ω, a_v, and a_q are virtual inputs to be designed and will differ according to the considered phase. We use the *hat* notation to emphasize that the the computation of $\widehat{H}$ and $\hat{c}$ is based on nominal values of the parameters which will be different from the true ones. When assuming $\hat{c} = c$ and $\widehat{H} = H$ and then substituting (8) into (6), the resulting base attitude (A), base position (P) and joint dynamics (J) are simplified as follows:

$$(A) \quad \dot{R}_0 = R_0 S(\omega_0) \qquad \dot{\omega}_0 = a_\omega \tag{9}$$

$$(P) \quad \dot{r}_0 = R_0 v_0 \qquad \dot{v}_0 = a_v \tag{10}$$

$$(J) \quad \dot{q} = \omega_q \qquad \dot{\omega}_q = a_q, \tag{11}$$

The main source of nonlinearity in (9)-(10) is related to the attitude kinematics (A), which is nonlinear due to the nature of the manifold of rotations SO(3).

As the ultimate goal is trajectory tracking, the dynamics is first rewritten using the following tracking error coordinates:

$$(A) \quad R_0^e = R_0^{d\top} R_0, \qquad \omega_0^e = \omega_0 - R_0^{e\top} \omega_0^d, \tag{12}$$

$$(P) \quad r_0^e = r_0 - r_0^d, \qquad v_0^e = R_0 v_0 - v_0^d, \tag{13}$$

$$(J) \quad q^e = q - q^d, \qquad \omega_q^e = \omega_q - \omega_q^d. \tag{14}$$

The error dynamics to be considered is then given by:

$$(A) \quad \begin{cases} \dot{R}_0^e = R_0^e S(\omega_0^e) \\ \dot{\omega}_0^e = a_\omega - S(\omega_0^e) R_0^e \omega_0^d - R_0^{e\top} \dot{\omega}_0^d \end{cases} \tag{15}$$

$$(P) \quad \begin{cases} \dot{r}_0^e = v_0^e \\ \dot{v}_0^e = R_0 (a_v + S(\omega_0) v_0) - \dot{v}_0^d \end{cases} \tag{16}$$

$$(J) \quad \begin{cases} \dot{q}^e = \omega_q^e \\ \dot{\omega}_q^e = a_q - \dot{\omega}_q^d. \end{cases} \tag{17}$$

We first address the position (P) and joint (J) error dynamics, which are characterized by second order linear dynamics upon using suitable preliminary inputs. Specifically, consider the following virtual inputs:

$$a_v = R_0^\top \left(-S(\omega_0) v_0 + \dot{v}_0^d + \gamma_p \left(r_0^e, v_0^e \right) \right) \tag{18}$$

$$a_q = \ddot{q}^d + \gamma_q \left(q^e, \dot{q}^e \right) \tag{19}$$

where $\gamma_p : \mathbb{R}^3 \times \mathbb{R}^3 \mapsto \mathbb{R}^3$ and $\gamma_q : \mathbb{R}^N \times \mathbb{R}^N \mapsto \mathbb{R}^N$ are feedback stabilizers yet to be designed. When substituting (18) and (19) into (16) and (17), the error dynamics reads:

$$(P) \quad \begin{cases} \dot{r}_0^e = v_0^e \\ \dot{v}_0^e = \gamma_p \left(r_0^e, v_0^e \right) \end{cases} \tag{20}$$

$$(J) \quad \begin{cases} \dot{q}^e = \omega_q^e \\ \dot{\omega}_q^e = \gamma_p \left(q^e, \dot{q}^e \right). \end{cases} \tag{21}$$

Defining $x^e := (r_0^e, q^e)$ and $v^e := (v_0^e, \omega_q^e)$ and considering a decentralized stabilizer $\gamma_x \left(x^e, v^e \right) = \left(\cdots, \gamma_{x_i} \left(x_i^e, v_i^e \right), \cdots \right)$, the error dynamics is made by $3 + N$ second order systems of the form

$$\dot{x}_i^e = v_i^e \tag{22}$$

$$\dot{v}_i^e = \gamma_{x_i}\left(x_i^e, v_i^e\right). \tag{23}$$

Each stabilizer γ_{x_i} is selected leveraging the quasi time-optimal solution proposed in [20]:

$$\gamma_{x_i}\left(x_i^e, v_i^e\right) = -\text{sat}_{b_i}\left(k_{x_i}\left(x_i^e + v_i^e \max\left(\frac{|v_i^e|}{2b_i}, \frac{k_{v_i}}{k_{x_i}}\right)\right)\right), \tag{24}$$

where $\text{sat}_{b_i}(x_i) = \min(\max(-b_i, x_i), b_i)$ is the standard saturation function, with $b_i > 0$ denoting the i-th saturation limit, while $k_{x_i}, k_{d_i} > 0$ are scalar PD-like gains. Notably, the proposed solution acts as a PD-like controller when far from actuator saturation, while it provides a time-optimal bang-bang response during saturation.

For the position and joint angles dynamics, we have the following result.

Theorem 1 *Given any smooth desired trajectory* $t \mapsto (r_0^d(t), q^d(t)) \in \mathbb{R}^{3+N}$ *and the corresponding velocity* $t \mapsto (v_0^d(t), \omega_q^d(t)) \in \mathbb{R}^{3+N}$ *for the base position and joint angles, respectively, the controller* (18)-(19) *makes the zero tracking error a Globally Asymptotically Stable (GAS) equilibrium point for the dynamics* (16)-(17).[†]

The proof is omitted as it follows automatically by using the result in [20, Lemma 2].

Since the QTO approach is designed for second-order *linear* dynamics, it cannot be applied for attitude control purposes. To ensure a bounded virtual input, we propose the following saturated control law:

$$a_\omega := -\text{sat}_{b_\omega}(K_{d,a}\omega_0^e) - \gamma_R(K_{p,a}R_0^e) + R_0^{e\top}\dot{\omega}_0^d \tag{25}$$

where

$$\gamma_R(K_{p,a}R_0^e) := \frac{1}{2}S^{-1}\left(\text{skew}(K_{p,a}R_0^e)\right), \tag{26}$$

is a nonlinear attitude error [27] and $\text{sat}_{b_\omega}(x) = (\text{sat}_{b_{\omega_1}}(x_1), \text{sat}_{b_{\omega_2}}(x_2), \text{sat}_{b_{\omega_3}}(x_3))$ is the element-wise saturation function. Each component of vector $b_\omega \in \mathbb{R}^3$ represents the bound applied to the corresponding angular velocity error feedback component. Noting that $\gamma_R(\cdot)$ is bounded by definition, the components of b_ω can be chosen sufficiently small to ensure that the control action a_ω remains bounded below a given value. Finally, the matrices $K_{p,a},\ K_{d,a} \in \mathbb{R}^{3\times3}$ are the proportional and derivative gains for the attitude, respectively, with $K_{p,a}$ satisfying $\text{trace}(K_{p,a})I_3 - K_{p,a} > 0$ [27].

Theorem 2 *Given any desired attitude trajectory* $t \mapsto R_0^d(t) \in \text{SO}(3)$ *and the corresponding angular velocity*

[†]Due to the topology of $\mathbb{S}^1$, to achieve global asymptotic stability with the proposed control law for the joint angles dynamics, a discontinuous (or a hybrid) controller must be employed. In particular, the proportional contribution q^e should be intended as $\text{atan2}(\sin(q^e), \cos(q^e))$ [26].

$\omega_0^d(t) \in \mathbb{R}^3$, *the controller* (25) *makes the error* $R^e = I_3, \omega^e = 0$ *an* Almost *GAS (AGAS)*[‡] *equilibrium point for the error dynamics* (15). *Moreover, sublevel sets of the form* $\left\{(R_0^e, \omega_0^e) \in \mathrm{SO}(3) \times \mathbb{R}^3 : \frac{1}{2} tr(K_{p,a}(I_3 - R_0^e)) + \frac{1}{2}|\omega_0^e|^2 \leq \ell\right\}$, *where* $\ell < \lambda_{min}(trK_{p,a}I_3 - K_{p,a})$ *are contained in the region of attraction.*

Proof *The proof will be conducted using a Lyapunov-based approach and is kept short as it follows arguments similar to those in [27]. First, note that the closed-loop attitude error dynamics is characterized by the following system of nonlinear differential equations on* $\mathrm{SO}(3) \times \mathbb{R}^3$*:*

$$\begin{aligned} \dot{R}_0^e &= R_0^e S(\omega_0^e) \\ \dot{\omega}_0^e &= -sat_{b_\omega}(K_{d,a}\omega_0^e) - \gamma_R(K_{p,a}R_0^e) + S(\omega_0^e)R_0^{e\top}\omega_0^d(t) \end{aligned} \tag{27}$$

which has four equilibrium points, one at the desired orientation $R_0^e = I_3$, $\omega_0^e = 0$ *and other three located at* $R_0^e = exp(\pi S(s))$, *where* $s \in \{e_1, e_2, e_3\}$, *which correspond to* π *rad rotations about each of the desired axes. To study the stability properties of the desired equilibrium, we consider the following Lyapunov candidate function:*

$$V := \frac{1}{2} tr(K_{p,a}(I_3 - R_0^e)) + \frac{1}{2}|\omega_0^e|^2 \tag{28}$$

where $tr(\cdot)$ *is the trace operator. Function V is positive definite and quadratic with respect to* ω_0^e *and* $\gamma_R(K_{p,a}R_0^e)$. *The Lie derivative of V along the error dynamics* (27) *reads:*

$$\dot{V} = \omega_0^{e\top}\gamma_R(K_{p,a}R_0^e) + \omega_0^{e\top}(-sat_{b_\omega}(K_{d,a}\omega_0^e) - \gamma_R(K_{p,a}R_0^e) + S(\omega_0^e)R_0^{e\top}\omega_0^d), \tag{29}$$

from which the expression $\dot{V} = -\omega_0^{e\top}sat_{b_\omega}(K_{d,a}\omega_0^e) \leq 0$ *is easily retrieved, which implies that the Lie derivative is negative semidefinite,* i.e., $\dot{V} \leq 0\ \forall (R_0^e, \omega_0^e) \in \mathrm{SO}(3) \times \mathbb{R}^3$. *By [29, Theorem 4.8], the desired equilibrium is uniformly stable. Since the Lie derivative is only negative semidefinite and the dynamics is time-varying (note the dependency on* $\omega_0^d(t)$ *in* (27)*), LaSalle/Yoshizawa [29, Theorem 8.4] theorem must be employed to claim that along the closed-loop trajectories* $\lim_{t\to\infty} \omega_0^e(t) = 0$. *This is not sufficient to state that the attitude asymptotically converges to the desired equilibrium. However, it is possible to demonstrate that the desired equilibrium is AGAS by first noting that system is asymptotically autonomous because* $\omega_0^e \to 0$ *implies* $S(\omega_0^e)R_0^{e\top}\omega_0^d(t) \to 0\ \forall \omega_0^d(\cdot)$. *Therefore, the closed-loop solutions will converge to the largest (pseudo) invariant set contained in* $E := \left\{(R_0^e, \omega_0^e) \in \mathrm{SO}(3) \times \mathbb{R}^3 : \omega_0^e = 0\right\}$, *which corresponds to the four equilibrium points of* (27). *Then, AGAS of the desired equilibrium point follows by showing that such a point is locally asymptotically stable while the three additional equilibria of* (27) *are hyperbolic.*

[‡]The concept of AGAS equilibrium point is a formal stability property that ensures the considered equilibrium is the unique locally asymptotically stable point of the system, and that trajectories starting from almost all initial conditions converge to it. AGAS essentially implies that the set of initial conditions not converging to the desired equilibrium has measure zero. For the case at hand, the undesired equilibria correspond to π rad rotations about each of the desired axes, very far from the nominal operating conditions. A more formal definition of AGAS can be found in [28].

This result can be achieved either by employing linearization or by means of Chetaev theorem, as done in [30]. The final part of the Theorem can be proven noting that the considered sublevel set of the Lyapunov function contains only the desired equilibrium.

Theorem 1 and Theorem 2 provide a formal certification of the tracking properties of our joint-space controller, with particular attention to the boundedness of the control action and the domain of attraction. This is especially relevant not only in the presence of large errors that may not be adequately handled by the guidance part but also for high performance tuning of the control parameters combined with limited actuation capabilities

C. Coordinated control design: post-capture phase

In the post-capture phase, a different control law must be considered since the objective is solely to cease the relative motion between the chaser and the target, bringing the whole system into a safe configuration with the base pointing in a desired absolute direction. Hence, the control law must be able to regulate only the attitude of the base and the joint angles of the manipulator, while allowing the entire system to undergo translations freely. Attitude regulation enables the execution of detumbling maneuvers, while joint angle control ensures the robotic arm reaches a safe configuration. This arrangement prevents undesired contacts between the arm and the satellite, and ensures that joint loads remain within safe operational limits. The desired attitude of the base and the desired joint angles, denoted by R_0^d and q^d respectively, are assumed to be constant setpoints provided by the guidance function.

To address this regulation task, we propose two different control laws. The first one, inspired by [14], is a direct extension of the feedback linearization law used in the pre-capture phase, which can be applied when the inertial parameters are known with sufficient accuracy. The second one is based on a bounded PD law that does not require knowledge of the system inertial parameters — namely, mass and inertia — at all, thereby granting intrinsic robustness to the design.

Feedback linearization-based law.

The system dynamics is first simplified by removing the uncontrolled degrees of freedom, related to the translational motion. By expanding the terms of the mass matrix and of Coriolis term in (6) as follows

$$H = \begin{bmatrix} H_r & H_{tr}^\top & H_{rm} \\ H_{tr} & H_t & H_{tm} \\ H_{rm}^\top & H_{tm}^\top & H_m \end{bmatrix}, \quad c = \begin{bmatrix} c_\omega \\ c_v \\ c_q \end{bmatrix}, \tag{30}$$

the equations of motion can be rewritten as:

$$\begin{aligned} H_r\dot{\omega}_0 + H_{tr}^\top \dot{v}_0 + H_{rm}\dot{\omega}_q + c_\omega &= \tau_0, \\ H_{tr}\dot{\omega}_0 + H_t\dot{v}_0 + H_{tm}\dot{\omega}_q + c_v &= f_0, \\ H_{rm}^\top\dot{\omega}_0 + H_{tm}^\top\dot{v}_0 + H_m\dot{\omega}_q + c_q &= \tau_q. \end{aligned} \tag{31}$$

Considering that no force is exerted, *i.e.*, $f_0 = 0$, and then solving the second equation in (31) for $\dot{v}_0$ and substituting it back into the other two equations, the post-capture dynamics is governed by the reduced order dynamics:

$$H_{\text{red}}(q)\begin{bmatrix}\dot{\omega}_0 \\ \dot{\omega}_q\end{bmatrix} + c_{\text{red}}\left(\omega_0, v_0, \omega_q, q\right) = \begin{bmatrix}\tau_0 \\ \tau_q\end{bmatrix} \tag{32}$$

where

$$H_{\text{red}}(q) = \begin{bmatrix} H_r - H_{tr}^\top H_t^{-1} H_{tr} & H_{rm} - H_{tr}^\top H_t^{-1} H_{tm} \\ H_{rm}^\top - H_{tm}^\top H_t^{-1} H_{tr} & H_m - H_{tm}^\top H_t^{-1} H_{tm} \end{bmatrix} \tag{33}$$

$$c_{\text{red}}\left(\omega_0, v_0, \omega_q, q\right) = \begin{bmatrix} c_\omega - H_{tr}^\top H_t^{-1} c_v \\ c_q - H_{tm}^\top H_t^{-1} c_v \end{bmatrix} \tag{34}$$

are the reduced mass and Coriolis matrix, respectively.

The control law is then chosen as:

$$\begin{bmatrix}\tau_0 \\ \tau_q\end{bmatrix} = \widehat{c}_{\text{red}}\left(v_0, \omega_q, q\right) + \widehat{H}_{\text{red}}(q)\begin{bmatrix}a_\omega \\ a_q\end{bmatrix}, \tag{35}$$

where $\widehat{H}_{\text{red}} \in \mathbb{R}^{3+N\times 3+N}$ and $\widehat{c}_{\text{red}} \in \mathbb{R}^{3+N}$, are estimates of the reduced mass and Coriolis matrix, respectively. The inputs a_ω and a_q can then be selected as those in (25) and (19) with the terms corresponding to angular velocities set to zero. When $H_{\text{red}} = \widehat{H}_{\text{red}}$ and $c_{\text{red}} = \widehat{c}_{\text{red}}$ the dynamics is further simplified, and corresponds to the one reported in equation (9) and (11) for subsystem (A) and (J), respectively. Then, the tracking errors can be defined as in equations (12) and (14), and the corresponding error dynamics is exactly the same given by equations (15) and (17).

The stability results for the post-capture closed-loop system can be derived along the lines of those for the pre-capture phase. Notably, we can readily prove that any desired trajectory for the joint angles is GAS and any desired attitude for the base is AGAS.

Lyapunov-based design.

In case the inertial parameters of the target are not known very accurately, a different solution is suggested to ensure robust regulation of the whole stack. Notably, the proposed solution does not need knowledge of the system inertial parameters.

For the derivation of the control law, we focus on the error dynamics

$$\dot{R}_0^e = R_0^e S(\omega_0) \tag{36}$$

$$\dot{q}^e = \omega_q \tag{37}$$

$$H(q)v = -C(v,q)v + \begin{bmatrix} \tau_0 & 0 & \tau_q \end{bmatrix}^\top, \tag{38}$$

where $C(v,q)v := c(v,q)$ is the Coriolis/centrifugal term expressed in convective form, leaving out the translation kinematics which is not controlled and decoupled from the other equations.

To regulate the attitude and the joint angles at the desired setpoint, the base and joint torque control input are specified according to the following bounded nonlinear PD laws:

$$\begin{aligned} \tau_0 &= -\mathrm{sat}_{b_\omega}(K_{d,a}\omega_0) - \gamma_R(K_{p,a}R_0^e) \\ \tau_q &= -\mathrm{sat}_{b_q}(K_{d,j}\omega_q) - K_{p,j}q^e, \end{aligned} \tag{39}$$

where $K_{d,a}$, $K_{d,j}$, $K_{p,a}$ and $K_{p,j}$ are proportional gain errors. The next theorem is one of the most important results of the work, formally showing that bounded feedback can be used to detumble the whole stack without knowledge of the system inertia, which is particular relevant in face of the potential uncertainty of the inertial properties of the chaser spacecraft.

Theorem 3 *Given any desired attitude R_0^d and any desired joint angles q^d setpoints, all the forward solutions $R_0(t)$, $q^e(t)$, $\omega_0(t)$, $v_0(t), \omega_q(t)$, $t \geq 0$, of the system* (36)-(38) *in closed loop with the control law* (39) *are bounded, and $(\omega_0(t), \omega_q(t), q^e(t))$ converge to zero globally, while $R_0^e(t)$ converges to I_3 from almost all initial conditions.*

Proof *We first note that the considered closed-loop system has the following equilibrium set*

$$A := \left\{ (v, R_0^e, q^e) : \omega_0 = 0,\, \omega_q = 0,\, e_0^e = 0\, q^e = 0 \right\},$$

which contains the desired attitude $R_0 = R_0^d$ and three other unwanted configurations, similarly to (27)*. The equilibrium set is characterized by constant linear speed motions ($v_0(t) = \bar{v}_0$). To prove the theorem, we make use of the Lyapunov*

function

$$V = \underbrace{v^\top H(q)v}_{\text{kinetic energy error}} + \underbrace{\frac{1}{2}tr(K_{p,a}(I_3 - R_0^e))}_{\text{attitude error potential}} + \underbrace{frac12{q^e}^\top K_{p,j}q^e}_{\text{joint angles error potential}} \tag{40}$$

where $v := (v_0, \omega_0, \omega_q) \in \mathbb{R}^{6+N}$*. The three terms of the function are, respectively: the kinetic energy error, the attitude error potential and the joint angles error potential.*

The Lie derivative of V along the flow of the system (36)-(38) *in closed loop with* (39) *reads:*

$$\begin{aligned}
\dot{V} &= v^\top H(q)\dot{v} + \frac{1}{2}v^\top \dot{H}(q)v + \omega_0^\top \gamma_R(K_{p,a}R_0^e) + \omega_q^\top K_{p,j}q^e \\
&= v^\top \left(\tfrac{1}{2}\dot{H}(q) - C(v,q)\right)v + v^\top(\tau_0, 0, \tau_q) \\
&+ \omega_0^\top \gamma_R(K_{p,a}R_0^e) + \omega_q^\top K_{p,j}q^e \\
&= v^\top(\tau_0, 0, \tau_q) + \omega_0^\top \gamma_R(K_{p,a}R_0^e) + \omega_q^\top K_{p,j}q^e \\
&= -\omega_0^\top sat(K_{d,a}\omega_0) - \omega_q^\top sat(K_{d,j}\omega_q) \leq 0,
\end{aligned} \tag{41}$$

$\forall (v, R_0^e, q^e) \in \mathbb{R}^{6+N} \times \mathrm{SO}(3) \times \mathbb{R}^N$*, where we exploited the well-known property that* $\frac{1}{2}\dot{H}(q) - C(v,q)$ *is skew-symmetric. From the positive definiteness of V about the point* $(v, R_0^e, q^e) = (0, I_3, 0)$ *and the global condition* $\dot{V} \leq 0$*, we immediately conclude forward completeness and boundedness of all the system solutions using standard arguments. Since the closed-loop dynamics is autonomous,* $\dot{V}$ *is negative semi-definite and all the conditions of LaSalle theorem [29, Theorem 4.4] are verified, we can conclude that all the solutions converge to the largest invariant set M contained in* $E := \left\{(v, R_0^e, q^e) : \omega_0 = 0,\, \omega_q = 0\right\}$, i.e.*, the set where* $\dot{V} = 0$*. To characterize M, pick a solution that belongs identically to E, namely, a solution characterized by* $\omega_0(t) = 0$ *and* $\omega_q(t) = 0\ \forall t \geq 0$*. Such a solution must satisfy*

$$H_{tr}^\top \dot{v}_0(t) = -\gamma_R(K_{p,a}R_0^e(t)), \tag{42}$$

$$H_t \dot{v}_0(t) = 0, \tag{43}$$

$$H_{tm}^\top \dot{v}_0(t) = -K_{p,j}q^e(t), \tag{44}$$

which implies $\gamma_R(K_{p,a}R_0^e(t)) = 0$ *and* $q^e(t) = 0$*. Therefore, the only solutions that can stay in E are those originating in the equilibrium set A, implying* $M \equiv A$*. Finally, the same arguments used in the final part of the proof of Theorem 1 can be exploited to show convergence of* R_0^e *to* I_3 *from almost all initial conditions.*

IV. Control law tuning

The primary limitation of the feedback linearization-based design lies in its dependence on precise knowledge of system parameters and dynamics, a requirement that is often questionable. Although stability is theoretically assured

even in the presence of small parametric errors [29, Lemma 13.4], achieving satisfactory tuning becomes challenging when incorporating additional dynamics such as actuators, sensors, sloshing and uncertainties like parametric variations and disturbances. This challenge is compounded by the numerous gains inside the control law. Building upon prior work [7], we exploit the absence of constraints on the gains of the proposed nonlinear control laws to employ an H_∞ synthesis approach on the linearized closed-loop system. This procedure systematically determines gain values ensuring local stability and desired performance levels when considering additional effects beyond the rigid body model (7).

Plant and control law linearization.

To perform the synthesis, both the plant and the controller must be linearized about a reference trajectory. The capture instant is selected as the operating point, therefore the dynamic matrices are treated as constant. Considering the plant dynamics in equation (6), the perturbed state is defined as follows:

$$\delta x := (\delta\alpha, \delta r_0, \delta q, \delta\omega_0, \delta v_0, \delta\omega_q) \tag{45}$$

where the symbol δ indicates the small variation of a variable with respect to a reference configuration ($\delta\alpha \in \mathbb{R}^3$ is a vector collecting three small angles describing the rotation between the desired and actual configuration). The kinematic matrix $A_{kin} = \text{blkdiag}(I_3, R_0^d, I_7) \in \mathbb{R}^{6+N\times 6+N}$, and the vector $u = (\delta\tau_0, \delta f_0, \delta\tau_q) \in \mathbb{R}^{6+N}$ are introduced as well, and the linearized equations of motion are written as:

$$\dot{\delta x} = \begin{bmatrix} 0 & A_{kin} \\ 0 & 0 \end{bmatrix} \delta x + \begin{bmatrix} 0 \\ \tilde{H}^{-1} \end{bmatrix} u. \tag{46}$$

The linearized model of equation (46) does not account for external perturbations, such as orbital disturbances, addressed in a previous work [4], which were found to have minimal impact due to the due to the fact that orbital disturbances are several orders of magnitude smaller than the control actions. Instead, this work focuses on the study of sloshing effects which were responsible for loss of performance when not properly accounted for. Hence, the matrices of the linearized model $\tilde{H} \in \mathbb{R}^{6+N\times 6+N}$ and $\tilde{c} \in \mathbb{R}^{6+N}$ are calculated according to the procedure outlined hereafter. First of all, the dynamics of the augmented system (7), that includes sloshing contribution, is expanded as follows:

$$\begin{cases} H_0\dot{\nu}_0 + H_{0m}\dot{\omega}_q + H_{0p}\dot{\omega}_p + c_0 = \begin{bmatrix} \tau_0 \\ f_0 \end{bmatrix} \\ H_{0m}^\top \dot{\nu}_0 + H_m\dot{\omega}_q + c_q = \tau_q \\ H_{0p}^\top \dot{\nu}_0 + H_p\dot{\omega}_p + c_p = 0 \end{cases} \tag{47}$$

where $\nu_0 := (\omega_0, v_0)$ is the twist of the base (a $6D$ vector collecting the body angular and linear velocity), $H_0 = \begin{bmatrix} H_r & H_{tr}^\top \\ H_{tr} & H_t \end{bmatrix}$, $c_0 = \begin{bmatrix} c_\omega \\ c_v \end{bmatrix}$, $H_{0m} = \begin{bmatrix} H_{rm} \\ H_{tm} \end{bmatrix}$, and H_p, c_p and H_{0p} are the additional terms coming from the augmentation of the system. By solving the last row of the system (47) for $\dot{\omega}_p$, and substituting back, the following new system matrices are obtained:

$$\tilde{H} = \begin{bmatrix} H_0 - H_{0p} H_p^{-1} H_{0p}^\top & H_{0m} \\ H_{0m}^\top & H_m \end{bmatrix} \tag{48}$$

$$\tilde{c} = \begin{bmatrix} c_0 - H_{0p} H_p^{-1} c_p \\ c \end{bmatrix}. \tag{49}$$

Then, the dynamics of the system can be compactly rewritten as:

$$\tilde{H} \begin{bmatrix} \dot{v}_0 \\ \dot{\omega}_q \end{bmatrix} + \tilde{c} = \begin{bmatrix} \tau_0 \\ f_0 \\ \tau_q \end{bmatrix}. \tag{50}$$

As recalled at the beginning of the section, the matrix $\tilde{H}$ and the term $\tilde{c}$ are evaluated at a specific operating point. Finally, the system is augmented with actuators and sensors dynamics. The former are described with a Padé approximation of a first-order filter $Del_{act} = \exp(-s\tau_{act})$, with $\tau_{act} = 0.1$ chosen as a reasonable value for actuators bandwidths. The actuator block is defined as:

$$Act. = \text{blkdiag}(Del_{act} I_3, Del_{act} I_3, Del_{act} I_7) \tag{51}$$

The sensors are described using a Padé approximation of a first-order filter, to model the delay as well. Specifically, a time constant $\tau_{bas} = 0.1$ s is selected for the base, and $\tau_{man} = 0.005$ s is chosen for the manipulator. Such values are selected based on the update rates of the onboard sensors (the cameras are assuming delivering images at 10 fps, while encoders delays are almost negligible). Thus, the delays $Del_{bas} = \exp(-s\tau_{bas})$ and $Del_{man} = \exp(-s\tau_{man})$ are included in the sensor block as follows:

$$Sens. = \text{blkdiag}(Del_{bas} I_3, Del_{bas} I_3, Del_{man} I_7, Del_{bas} I_3, Del_{bas} I_3, Del_{man} I_7) \tag{52}$$

For the post-capture dynamics, the linearized model is obtained from (32) neglecting the Coriolis/centrifugal term.

Once the linear models are obtained, uncertainties are incorporated into the model using the Linear Fractional Transformation (LFT) form. Specifically, the inertial uncertainties related to mass, moments of inertia, products of inertia, as well as initial conditions and center of mass position of both chaser and target spacecraft are considered,

modeled as multiplicative deviations from the nominal value, according to the values reported in Section VI.A. The LFT diagram is illustrated in Figure 3, having defined $z = (z1, z2)$ as exogenous output, including performance outputs, and $w = (n, d)$ as exogenous input, including noise and disturbances. Moreover, the uncertainties are collected in the vector Δ, while M is the nominal model of the plant.

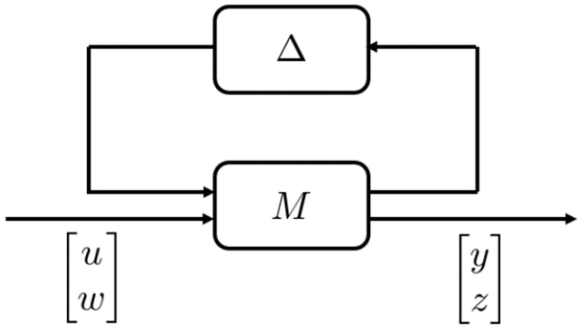

Fig. 3 Uncertain plant in LFT form.

The controller is linearized by retaining the proportional derivative contribution of the virtual inputs. In the pre-capture phase the linearized control law is

$$\begin{bmatrix} \delta\tau_0 \\ \delta f_0 \\ \delta\tau_q \end{bmatrix} = \widehat{H}_{\text{lin}} \begin{bmatrix} K_{p,a} & 0 & 0 & K_{d,a} & 0 & 0 \\ 0 & K_{p,p} & 0 & 0 & K_{d,p} & 0 \\ 0 & 0 & K_{p,j} & 0 & 0 & K_{d,j} \end{bmatrix} \delta x, \tag{53}$$

while in the post-capture phase it is given by:

$$\begin{bmatrix} \delta\tau_0 \\ \delta\tau_q \end{bmatrix} = \widehat{H}_{\text{red,lin}} \begin{bmatrix} K_{p,a} & 0 & K_{d,a} & 0 \\ 0 & K_{p,j} & 0 & K_{d,j} \end{bmatrix} \begin{bmatrix} \delta\alpha \\ \delta q \\ \delta\omega_0 \\ \delta\omega_q \end{bmatrix} \tag{54}$$

where $K_{p,a}$, $K_{d,a}$, $K_{p,p}$, $K_{d,p}$ and $K_{p,j}$, $K_{d,j}$ are diagonal gain matrices depending on the control law and the corresponding phase of mission. Thanks to the nonlinear preliminary feedback linearizing law (8), the closed-loop system is transformed into decoupled subsystems, making possible to exploit the presented structure in the control laws. Similarly to the matrices of the linearized plant, $\widehat{H}_{\text{lin}}$ and $\widehat{H}_{\text{red,lin}}$ are evaluated by considering, respectively, $\widehat{H}$ and $\widehat{H}_{\text{red}}$

at a specific operating point. However, it is worth highlighting that these terms depend on the nominal values of the plant parameters.

Control synthesis.

Once both the plant and the controller dynamics have been linearized, the controller synthesis is performed using an H_∞ synthesis procedure. Specifically, the mixed-sensitivity approach proposed in [21] is adopted and here briefly presented to make the work self-contained.

Let $K(s, \theta)$ be a structured linearized controller represented in the Laplace domain, dependent on a vector of tunable parameters $\theta \in \mathbb{R}^{n_\theta}$, and let $J_i(\theta), i = 1, \ldots, n$ be a set of n objectives

$$J_i(\theta) = \|W_i(s)S_i(s, \theta)\|_\infty \tag{55}$$

where $S_i(s, \theta)$ is the transfer function from some performance input to some performance output of the closed-loop plant and $W_i(s)$ is the corresponding frequency weight. Such weights are representative of specific objectives. For the capturing phase, the requirements imposed are the following:

- Req. 1: Tracking performance requirement from base pose setpoint to base pose error.
- Req. 2: Tracking performance requirement from joint angles setpoint to joint angles.
- Req. 3: Control effort moderation from base and joint setpoints to base control wrench.
- Req. 4: Control effort moderation from base and joint setpoints to arm torque commands.

Such objectives are translated into frequency weights with a block diagonal structure $W_S(s) = \text{blkdiag}(W_{S,a}, W_{S,p}, W_{S,j})$ and $W_Q(s) = \text{blkdiag}(W_{Q,a}, W_{Q,p}, W_{Q,j})$. Tracking performance weights are modeled as first order filters of the form $W(s) = \frac{\frac{s}{M} + \omega_c}{s + A\omega_c}$, having defined a low frequency gain A such that $W(0) = \frac{1}{a}$ and an high frequency gain M such that $W(\infty) = \frac{1}{M}$, using the function `makeweight`, according to the cross over frequencies (ω_c) reported in Section VI.B. Control effort weights are chosen as unitary weights. In the post-capture phase, instead, the following objectives are considered:

- Req. 5: Tracking requirement from base attitude setpoint to base attitude error.
- Req. 6: Tracking performance requirement from joint angles setpoint to joint angles error.
- Req. 7: Control moderation requirement from base and manipulator setpoint to base torque command.
- Req. 8: Control moderation requirement from base and manipulator setpoint to arm torque command.

Analogously to the capture phase, the requirements are translated into frequency weights: $W_{S,PC}(s) = \text{blkdiag}(W_{S,a}, W_{S,j})$ and $W_{Q,PC}(s) = \text{blkdiag}(W_{Q,a}, W_{Q,j})$. Cross over frequencies are indicated in Section VI.

In the SISO case, the inverse of the magnitude of weight can be interpreted as the desired shape, or template, for the magnitude of the frequency response to be shaped.

The mixed-sensitivity synthesis can then be cast as the problem of finding the parameter vector θ which solves the following multi-objective optimization problem:

$$\begin{aligned} &\min_{\theta} \max_{i=1,\dots,n} J_i(\theta) \\ &\text{subject to} \\ &\max_{j=1,\dots,c} H_j(\theta) \end{aligned} \tag{56}$$

while guaranteeing that the closed-loop system is stable. The constrained optimization in (57) accounts for c inequality constraints of the form

$$H_j(\theta) = \left\| W_j(s) S_j(s,\theta) \right\|_\infty \quad H_j(\theta) \leq 1, \quad j = 1, \dots, c. \tag{57}$$

The optimization problem stated above is implemented in the MATLAB `systune` routine. Given an open-loop plant $G(s)$, to ensure consistency in the computation of the norm of a linear multi-variable system, it is important to normalize the inputs and outputs of $G(s)$. The open-loop plant is typically replaced with $G'(s) = Y^{-1}G(s)U$. Here, Y and U are constant diagonal matrices of appropriate dimensions, and their inverses scale the inputs and outputs of G, respectively. In particular, U is selected so that the maximum allowed control input is normalized to 1. This is achieved by setting the diagonal entries of U as the maximum available control input for the corresponding channel. Y normalizes the output to 1, and its precise value is determined through an iterative procedure. The objective of the synthesis process is to find a controller $K'(s)$ such that $u = K'(s)y$ solves the optimization problem (57). The controller to be implemented on the unscaled plant is obtained as $K = UK'Y^{-1}$.

After performing the synthesis, robust stability is assessed using `robstab` routine implemented in MATLAB. The results are reported in Section VI, while μ-plots are reported in Figure 4, terms of evaluated upper and lower bounds of the stability margins. The figure is referred to the scenario 2, that is more challenging.
A weight $W_Y(s)$, modeled as a first-order filter with a structure analogous to $W_S(s)$, the same cross-over frequency, and frequency weights reported in Section VI. It is used in the robust stability routine as a weight for the output.

The architecture of the complete setup of the synthesis process is reported in Figure 5. All the inputs are prefiltered with a constant gain for normalization purposes.

Synthesis results are provided in terms of singular values of sensitivity (Figure 6), complementary sensitivity (Figure 7) and control sensitivity (Figure 8). For brevity, only the results relative to the more challenging Scenario 2 are provided.

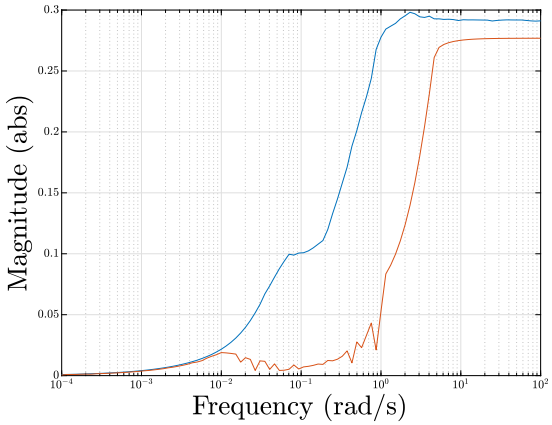

Fig. 4 Control loop architecture for synthesis.

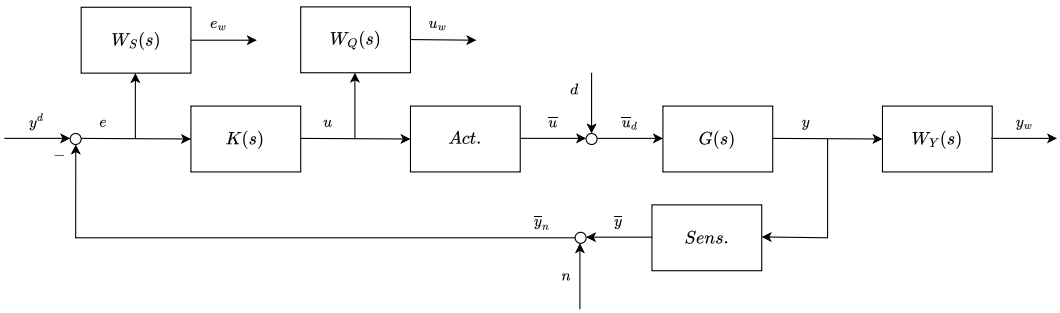

Fig. 5 Control loop architecture for synthesis.

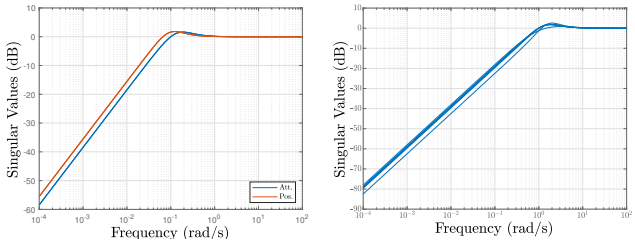

(a) **(b)**

Fig. 6 Singular values of the sensitivity for base (a) and manipulator(b).

V. Guidance Strategy

The guidance strategy aims at generating suitable trajectories for both the pre- and post- capturing task which are compatible with the control law presented in Section III. Following a classical guidance-control paradigm, the guidance is not included in the synthesis process. The strategy is straightforward for the post-capture phase, in which the objective is just to stop the relative motion between the manipulator and the base. In this case, the guidance function provides a

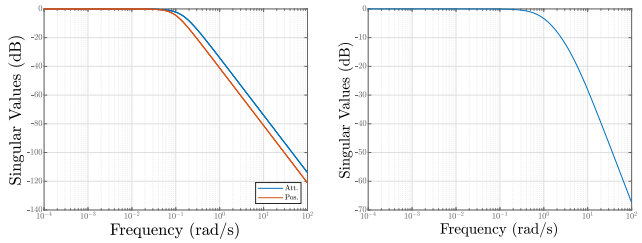

(a) **(b)**

Fig. 7 Singular values of the complementary sensitivity for base (a) and manipulator(b).

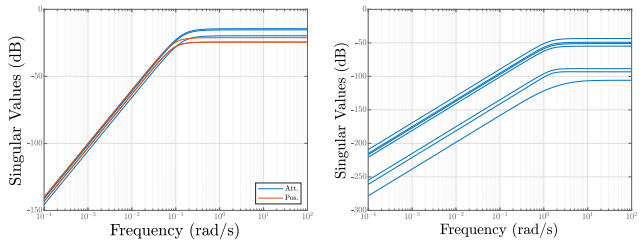

(a) **(b)**

Fig. 8 Singular values of the control sensitivity for base (a) and manipulator(b).

desired constant attitude R_0^d for the chaser base given the initial attitude and a desired constant configuration of the joints q^d, which ensures a safe final configuration for the overall stack (chaser+target). The position is left free as this degree of freedom is not controlled in this phase.

The pre-capture phase is more involved to be dealt with and we proceed assuming that the space robot in the pre-capture phase is close to the target, with a small relative distance and motion. We report here for completeness the main steps of the guidance algorithm as it is the same already adopted in [7].

The guidance of the base is obtained by selecting a proper fixed configuration $p_0^{sp} := (r_0^{sp}, R_0^{sp})$ and corresponding velocity v_0^{sp}, in the LVLH frame. Instead, given a desired grasping time t_g, the desired final pose $p_N^{sp}(t_g) := (r_N^{sp}(t_g), R_N^{sp}(t_g))$ and twist $v_N^{sp}(t_g)$ of the end-effector depends on the location and velocity of the grasping point at t_g. These quantities are predicted by propagating the target motion from the initial time t_0 forward up to t_g. Since the motion prediction of the target is only accurate for a short time horizon, the coefficients of the polynomial interpolation are updated at each step using current measurements of both the chaser and target states. This allows for a new prediction of the future motion of the grasping point. This approach compensates for variations in the expected location of the chaser's center of mass and the grasping point. As the time for grasping approaches, the prediction horizon for the grasping point location decreases, but the guidance is able to compensate for any mismatch in the final location of the grasping point. Then, the initial (measured) pose $p_N(t_0)$ and the final desired pose of the end-effector are interpolated using a 5-th order polynomial, providing a trajectory $t \mapsto p_N^d(t)$ for the end-effector (see Algorithm 1).

Once $p_N^d(t)$ is available, an inverse kinematics algorithm is employed to compute the joint coordinates guidance from end-effector pose trajectory. Inverse kinematics is usually complex, with solutions that can be multiple or, in some cases, nonexistent. When dealing with fixed-base robots, the existence of kinematic redundancy ($N > 6$) in the arm ensures that there are infinite solutions available. This, in turn, provides an opportunity to enhance performance by identifying and selecting the most suitable solution based on specific optimality criteria. The inverse kinematics is solved at the joint velocity level:

$$ {}^N\nu_N^d(t) = {}^N\nu_0(t) + J_N(q)\dot{q}^d, \tag{58} $$

where ${}^N\nu_N^d := ({}^N\omega_N^d, {}^N v_N^d)$ is the (desired) twist profile of the end-effector, ${}^N\nu_0$ is the twist of the base, both expressed in F_N,

$$ J_N(q) = \begin{bmatrix} {}^N X_1 \, {}^1X_{0,1}(q_1)s_r & \cdots & {}^N X_{N-1,N}(q_N)s_r \end{bmatrix}. $$

is the Jacobian of the end-effector, with

$$ {}^iX_j := \begin{bmatrix} {}^iR_j & 0_3 \\ S({}^ir_{ij})\,{}^iR_j & {}^iR_j \end{bmatrix}, \tag{59} $$

denoting the spatial transformation between frame i and j (see Figure 1) and $s_r := [0\,0\,1\,0\,0\,0]^\top$ denoting the motion subspace constraints [8] associated with revolute joints, aligned with the z axis. Solving (58) for $\dot{q}^d$:

$$ \dot{q}^d = J_N^\dagger(q)\left({}^N\nu_N^d - {}^N\nu_0\right) \tag{60} $$

where $J_N^\dagger(q) \in \mathbb{R}^{N\times 6}$ is the right pseudoinverse of the end-effector Jacobian matrix. Equation (60) represents the inverse kinematics solution of a floating robot, which accounts also for the base velocity $\nu_0 \in \mathbb{R}^6$.

At this point, a feedback term is added, following the work in [31], to compensate for possible position and attitude errors. Note that this approach has been extended to the spatial case, since the end-effector orientation is crucial for a correct capture execution, thus the error must be defined in terms of both position and orientation coordinates, as explained in [32] as well:

$$ p_N^e = \begin{bmatrix} r_N^d - r_N \\ \gamma_R(R_N^e) \end{bmatrix} \tag{61} $$

where $r_N^d \in \mathbb{R}^3$ and $r_N \in \mathbb{R}^3$ are, respectively, desired and current position of the end-effector, while $R_N^e \in \mathrm{SO}(3)$ is the

attitude error, defined as ${R_N^d}^\top R_N \in \mathrm{SO}(3)$. The closed-loop inverse kinematics equation becomes:

$$\dot{q}^d = J_N^\dagger(q)\left(\nu_N^d - {}^N\nu_0 + K_g p_N^e\right) \tag{62}$$

with K_g denoting a positive definite gain matrix of the form $K_g = \mathrm{diag}(k_{g,p}I_3, k_{g,a}I_3)$. Kinematic redundancy guarantees the existence of a subspace of joint-space velocities, corresponding to the *null space* of $J_N(q)$ which does not yield a velocity in the task space. Hence, the general solution to (58) is reformulated by including a self-motion of the manipulator, defined using a projection matrix:

$$\dot{q}^d = J_N^\dagger(q)\left(\nu_N^d - {}^N\nu_0 + K_g p_N^e\right) + (I_{6+N} - J_N^\dagger(q)J_N(q))\dot{q}^n. \tag{63}$$

A common approach to select $\dot{q}^n$ is through the projected gradient method, in order to maximize a performance index $w(q)$:

$$\dot{q}^n = k_0\left(\frac{\partial w\,(q)}{\partial q}\right)^\top \tag{64}$$

where $k_0 > 0$ is a scalar gain. Several possibilities exists on the choice of the function $w\,(q)$. Typically, functions maximizing robot dexterity [33] or avoiding mechanical joint limits [31] are chosen. For instance, if one chooses to maximize manipulability, a possible selection for w is:

$$w\,(q) = \det\left(\sqrt{J_N\,(q)\,J_N^\dagger\,(q)}\right). \tag{65}$$

The complete guidance algorithm is summarized in Algorithm 1: at each sampling instant of the guidance algorithm, a quintic polynomial trajectory from the current time to the grasping time is computed, for both base and end-effector's poses. First, the polynomial coefficients are generated and stored in the vectors coefs_0 (base pose) and coefs_N (end-effector's pose), by matching current and final conditions, using the function CoeffGen. Then, the actual trajectory is reconstructed by creating the polynomials and the corresponding derivatives using the function PolyTraj. Finally, pose and twist profiles are exploited to perform the inverse kinematics algorithm (function InvKin), according to equation (60), thus retrieving the desired joint rates. Desired joint angles and joint accelerations are then reconstructed by numerically integrating and deriving the obtained joint rates.

Algorithm 1 Guidance algorithm at each simulation step.

$t_{old} = 0$

for $t = t_0$ **to** t_g **do**

$\Delta t = t - t_{old}$

$\text{coefs}_0 = \text{CoeffGen}(t, t_g, p_0(t), p_0^{sp}, v_0^{sp})$

$\text{coefs}_N = \text{CoeffGen}(t, t_g, p_N(t), p_N^{sp}(t_g), v_N^{sp}(t_g))$

$[p_0^d(t), v_0^d(t), \dot{v}_0^d(t)] = \text{PolyTraj}(\text{coefs}_0, \Delta t)$

$[p_N^d(t), v_N^d(t)] = \text{PolyTraj}(\text{coefs}_N, \Delta t)$

$\dot{q}^d(t) = \text{InvKin}(v_0(t), p_N(t), p_N^d(t), v_N^d(t))$

$t = t_{old}$

end for

VI. Numerical Results

After a brief introduction to the two scenarios under consideration, in this section the results of the control synthesis approach are shown. Following that, the results of the nonlinear simulations conducted to assess the validity of the solution are presented for each phase. Simulation parameters have been randomly sampled from the uncertainty set reported in this section. In the pre-capture phase, a Monte Carlo study has been conducted, involving 100 simulations for each scenario, to verify the efficacy of the proposed control algorithm in more realistic conditions.

It is worth emphasizing that, in Scenario 1, the target is stationary (semi-collaborative), whereas in Scenario 2, it is tumbling and uncontrolled. Therefore, the case study of Scenario 1 should be understood as a validation in a much simpler and controlled situation, while the potential of the new controller is validated in the more challenging Scenario 2.

A. Scenarios Definition

Two different scenarios are considered, concerning In-Orbit Servicing (IOS) activities. The first one is the servicing of a large geostationary platform (SSL/1300), considered to be semi-collaborative and semi-cooperative. The second scenario involves a servicing mission of a small satellite within a large LEO constellation, such as the Airbus Arrow platform or the OneWeb constellation, which also serves as a representative model for other constellation configurations like IRIDIUM, GLOBALSAR, and Starlink. In this case the target is considered to be non collaborative and semi-cooperative [4, Table 1]. The chaser platform designed for the GEO scenario is derived from the literature [34], while the servicing satellite in the second scenario is taken from [35]. Physical data of the two satellites are reported in Table 1.

The general structure of the chaser spacecraft is common to the two scenarios. The main feature is a redundant ($N = 7$) and highly dexterous robotic manipulator, essential to correctly perform the capture. Moreover, the chaser

	Parameter	SC1	SC2
C	Mass [kg]	1900	372
	Bus dim. [m]	[2; 2.3; 3.1]	[1.3; 1.3; 1.7]
	SA dim. [m]	[11; 2.1; 0.01]	/
	MoI [kg m^2]	$[13.5;\ 2;\ 14] \times 10^3$	[200; 200; 140]
	PoI [kg m^2]	[0; 0; 0]	[0; 0; 0]
T	Mass [kg]	2000	150
	Bus dim. [m]	[2.5; 2.8; 3.5]	[1; 1; 1]
	SA dim. [m]	[14; 2.5; 0.01]	[1; 1; 0.01]

Table 1 Chasers and targets parameters

spacecraft is equipped with a complete set of sensors and actuators, to perform all the GNC functions. Specifically, the satellite base exploits a reaction control system, composed of a total of 24 thrusters, and four Reaction Wheels (RWs) in standard configuration, to fully control the spacecraft in both translation and rotation, while the robotic arm is commanded using brushless DC joint motors. The values of maximum action for every actuator are reported in Table 2.

Actuator	SC1	SC2
Reaction Wheel [Nm]	0.5	0.248
Thruster [N]	10	1
DC Motor [Nm]	10	25

Table 2 Actuators limits

Mass and inertia parameters — in terms of Moments of Inertia (MoI) and Products of Inertia (PoI) — of both chaser and target are considered uncertain for both scenarios. The position of the Center of Mass (CoM) of both satellites is considered uncertain as well. Furthermore, uncertainties in the initial conditions are considered, to address potential errors in the previous phases of the mission. The considered values are reported in Table 3. All the uncertainties reported apply along the three directions. Specifically, the uncertainties in the CoM position provide the offset between the geometrically fixed frame and the body frame.

The manipulator, as previously mentioned, is a robotic arm with 7 degrees of freedom. Its configuration is shown in Figure 9, and the lengths of the joints are specified as follows: $l_i = 19$ cm, $l_{off} = 16$ cm, $l_1 = 80$ cm, and $l_f = 21$ cm.

In both scenarios, the aim is the on-orbit refueling of two targets and, for this reason, the satellites are equipped with the tanks containing the propellant suitable for refueling purposes. Specifically, in Scenario 1, the chaser spacecraft is supposed to service a platform, with a bi-propellant propulsion system. Therefore, the chaser is equipped with two tanks, for the refueling of both fuel (Monomethil Hydrazine) and oxidizer (Nitrogen tetroxide). In Scenario 2, the

Parameter uncertainties	SC1	SC2
Chaser mass [%]	5	5
Target mass [%]	10	10
Chaser MoI [%]	10	10
Target MoI [%]	20	20
Chaser PoI $\left[\text{kgm}^2\right]$	100	1
Target PoI $\left[\text{kgm}^2\right]$	100	1
Chaser CoM position [m]	0.2	0.05
Target CoM position [m]	0.2	0.05
Chaser Initial position [m]	0.5	0.25
Target Initial position [m]	0.5	0.25

Table 3 Parameter uncertainties for chaser and target.

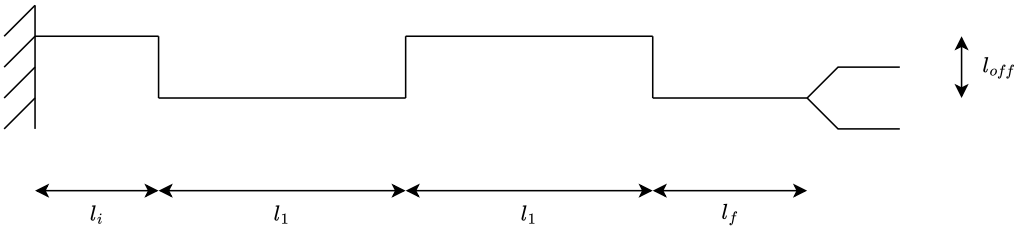

Fig. 9 Robotic arm configuration.

target uses monopropellant Hydrazine as a fuel, hence only one tank is present. As already said, the chaser platform design for the GEO scenario is derived from the literature and the total launch mass of the spacecraft is assumed to be 2500 kg, considering 400 kg of bipropellant, stored in two spherical tank, for refueling purposes, and 400 kg of propellant to reach the GEO orbit. The chaser is supposed to service two spacecraft and the scenario under study is located at the beginning of the second service, therefore considered a spacecraft mass of 1900 kg, with two half-filled tanks, each with 100 kg of fuel and oxidizer. The chaser spacecraft in the second scenario, has instead a wet mass of 500 kg and a dry mass of 245 kg. The spacecraft is supposed to refuel two targets as well, hence, by considering the conditions at the beginning of the second service, the total mass is estimated to be 372 kg, with 127 kg of propellant, stored in an half-filled spherical tank. Given propellant density and mass, the radius of the tank may be recovered in a straightforward manner. Hence, the pendulum models for the two scenarios are derived from fuel parameters. The values of length and mass of each equivalent pendulum are reported in Table 4.

	Length L_p [m]	Mass m_p [kg]
Hydrazine	0.39	127
Nitrogen Tetroxide	0.32	100
MMH	0.38	100

Table 4 Pendulum parameters.

Specifically, in Scenario 1, four additional degrees of freedom are added, having $n_t = 2$ and $q_p = (q_{t_1}, q_{t_2}) \in \mathbb{R}^4$, accounting for fuel and oxidizer tanks. In scenario 2, $n_t = 1$ and $q_p \in \mathbb{R}^2$ has the contribution of the only tank present.

B. Control synthesis results

Before showing the simulation outcomes, the results of the control synthesis are presented. Given the controller structure and the performance objectives, imposed as soft requirements (see Section IV), the results, in terms of worst-case tuning goals, for each of the objectives are reported in Table 5 (a value smaller than 1 implies that the objective is satisfied, values close to 1 are still acceptable). The controller has been tuned on the nominal system, by setting the desired bandwidth of the closed loop systems according to previous work present in the literature. Specifically, requirements in Scenario 1 are taken from [36] and, consequently, a bandwidth of 0.08 Hz is imposed to position and attitude closed loops, while a bandwidth of 0.16 Hz is set for the manipulator joints. Instead, the requirements for Scenario 2 are imposed looking at [37]: position and attitude setpoints are set to 0.03 Hz and 0.05 Hz, respectively, while the joints bandwidth is set to be 0.5 Hz. The robust stability of the controller has been assessed according to the uncertainties indicated in Table 3, and the results, in terms of lower bound (LB) and upper bound (UB) are reported in Table 5. A stability margin value of α indicates that the controller can withstand up to α times the specified uncertainties. If the lower bounds of the stability margin are greater than 1, it confirms robust stability. Conversely, if the upper bounds are less than 1, it indicates that the controller is not robust against the uncertainties within the considered set.

	Req. 1	Req. 2	Req. 3	Req. 4	LB	UB
SC1	1.0745	1.0745	1.0745	0.0186	5.8565	7.7430
SC2	1.5718	1.5718	1.5718	0.0065	3.4298	3.6311

Table 5 Achieved constraints values for the two scenarios.

Analogously, for the post-capture phase, the optimization cost achieved are reported in Table 6. In both scenarios,

the bandwidth of both base and arm closed loops requirements is set 0.01 Hz. Also in this case, satisfactory results are obtained. Additionally, stability margins have been computed, proving robust stability.

In all scenarios the weights for the sensitivity function are chosen as $a = 0.01$ and $M = 1.1$, while the weights for the complementary sensitivity are selected as $a = 1.1$ and $M = 0.01$.

	Req. 5	Req. 6	Req. 7	Req. 8	LB	UB
SC1	0.9740	0.9773	0.9314	0.0069	4.0122	10.0980
SC2	0.9856	0.9733	0.7636	0.0023	4.0055	8.2639

Table 6 Achieved constraints values for the two scenarios, post capture phase.

C. Pre-Capture Phase: Scenario 1

The pre-capture phase is characterized by a closing approach of the chaser with respect to the target. Once the former is sufficiently close, it is commanded to the satellite base to remain in a station-keeping position, while the manipulator performs the capture, leveraging the algorithms described in Section V. Specifically, in Scenario 1 the target is considered to be semi-collaborative, meaning that it is able to maintain an attitude profile, thus ensuring low residual angular rates of the target to aid approach and capture by the chaser.

The results of the Monte Carlo simulations are shown in terms of the norm of the end-effector pose error in Figure 10. For both position and attitude are displayed the mean values $\bar{p}^e_N$, $\bar{e}^e_N$ and standard deviation $\sigma^e_{p_N}$, $\sigma^e_{e_N}$. Furthermore, the mean and standard deviation of the spherical pendulum's position coordinates during the whole study, that represent the sloshing of the liquid inside the propellants, are shown in Figure 11. The control actions, in the nominal case, are reported in Figure 13, while the joint displacements are shown in Figure 12. It is worth noting that reaction wheels, which have limited control authority due to the considered saturation limits (see Table 2), become saturated during a large portion of the maneuver. Yet, the maneuver is successfully completed, and the oscillations induced by fuel sloshing are effectively counteracted with satisfactory performance.

D. Pre-Capture Phase: Scenario 2

The second scenario represents a more challenging case for the GNC system, since the target is non-collaborative and tumbling at a high rate (up to 2.5 deg/s), so that the chaser has to perform synchronization maneuvers in order to reduce the residual relative motion. Such maneuvers are not considered in the forthcoming simulations since the pre-capture phase begins after them, but uncertainties on the inital position are taken into account to address potential errors in the previous phase. The mean value and the standard deviation of the end-effector's pose error norm, is reported in Figure 14, while the joint displacements in the nominal case are displayed in Figure 15.

The control actions are reported in Figure 16, which shows again that reaction wheels reach the saturation bounds

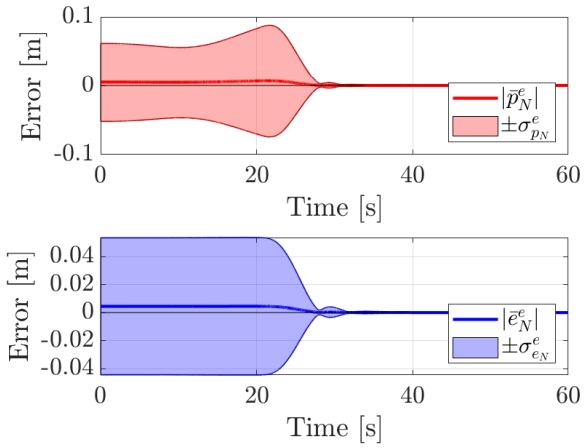

Fig. 10 End-effector's pose error norm - Scenario 1.

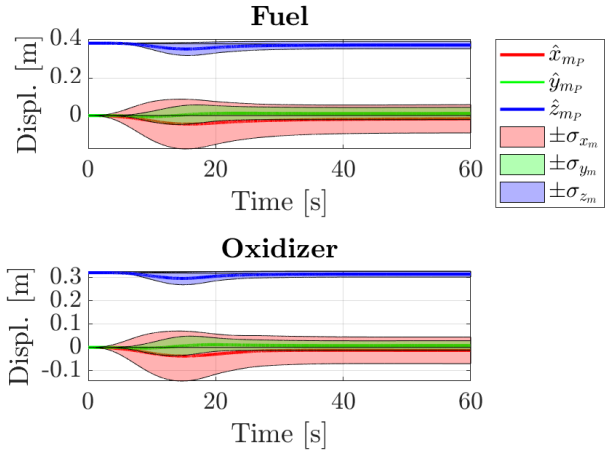

Fig. 11 Sloshing pendulum displacement - Scenario 1.

during the maneuver. Although actuators saturate during the maneuver, the proposed control law provides good tracking performance and ensures a successful capture.

For the sake of brevity, the results for what concerns sloshing mass displacement are not reported for Scenario 2, since it shows a similar behavior.

E. Post-Capture Phase: Scenario 1

The post-capture phase consists in the detumbling of the target, and the subsequent stabilization, to perform the servicing operations. Note that, in the scenario under study, the target is already nearly stationary during capture, hence a residual moment is introduced into the system, induced by contact. This residual moment must be promptly damped out by the post-capture control algorithm. Initial conditions of this phase are equal to the ones at the last instant of

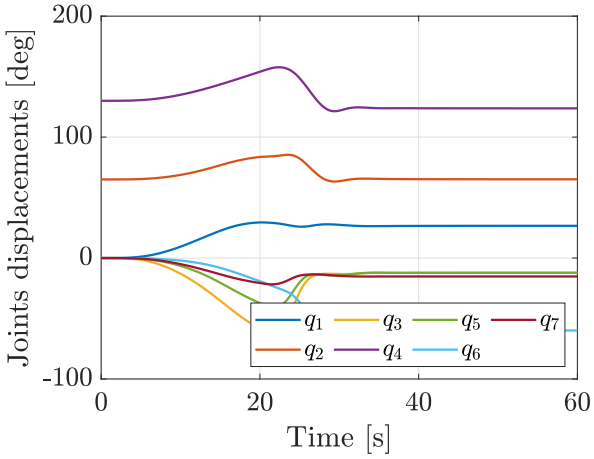

Fig. 12 Joint displacements - Scenario 1.

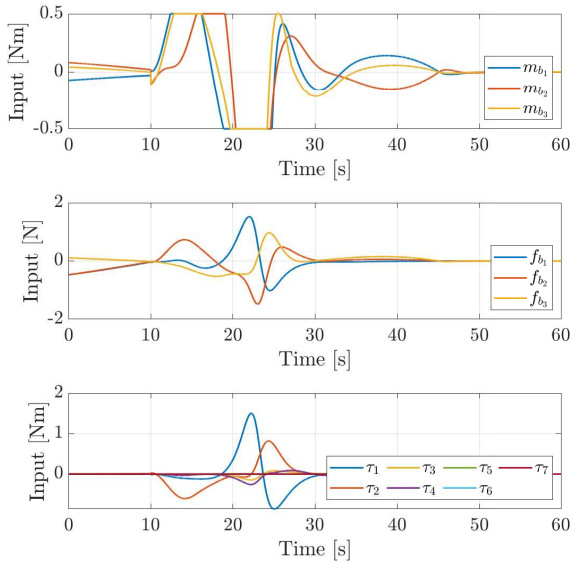

Fig. 13 Control actions - Scenario 1.

simulation of the pre-capture phase, thus neglecting contacts. Detumbling and stiffening are achieved by commanding a constant setpoint, corresponding to the current configuration, for the attitude of the base and joint angles of the manipulator. The results are reported in terms of joints displacements, in Figure 17, and control actions in Figure 18 (nominal case).

Once again, it is possible to see that the reaction wheels are pushed to their saturation limits. Nevertheless, stabilization of the system, and stopping of the relative motion, is achieved in reasonable time.

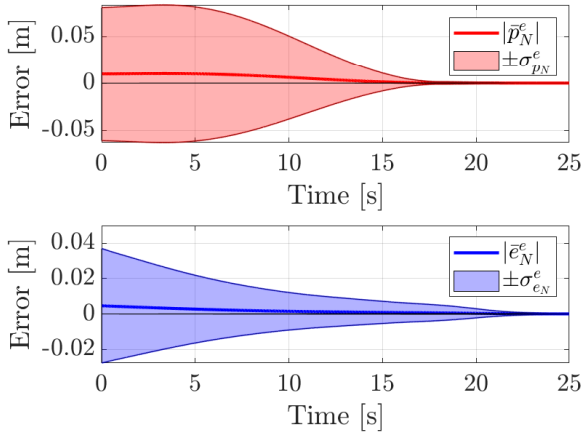

Fig. 14 End-effector's pose error norm - Scenario 2.

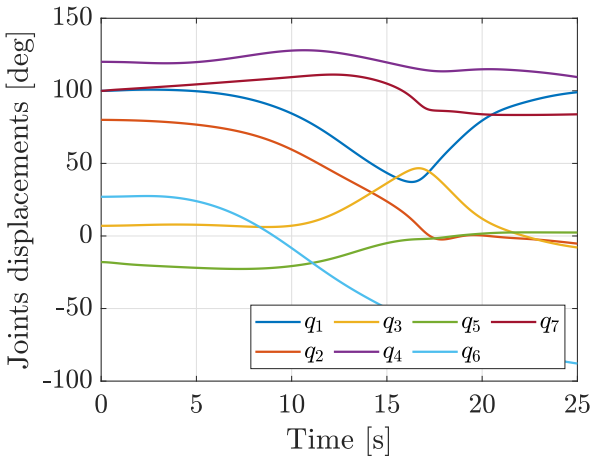

Fig. 15 Joint displacements - Scenario 2.

F. Post-Capture Phase: Scenario 2

The post-capture phase in the second scenario follows an approach totally analogous to the previous one. In the simulation, initial conditions of this phase are inherited from the ones at the last instant of pre-capture phase configuration, thus neglecting contacts. Greater simulation time is taken into account, due to higher tumbling rate of the target. Moreover, in this scenario a safe joint configuration is commanded, different from the current one. Looking at Figure 19 it is possible to appreciate that joints setpoint values are reached. Furthermore, to support the effectiveness of the proposed controller, control actions are reported in Figure 20.

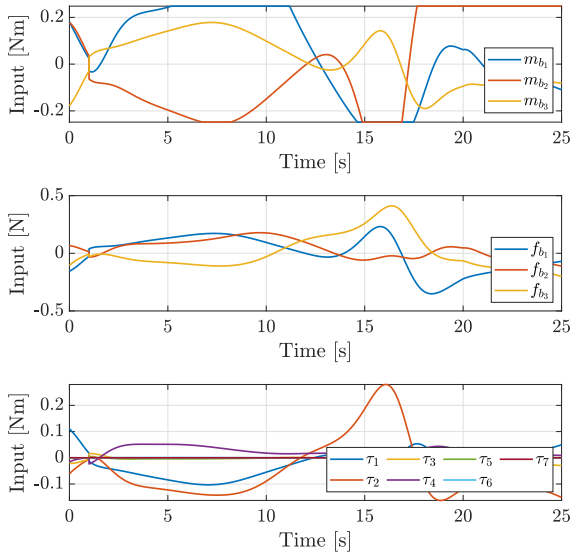

Fig. 16 Control actions - Scenario 2.

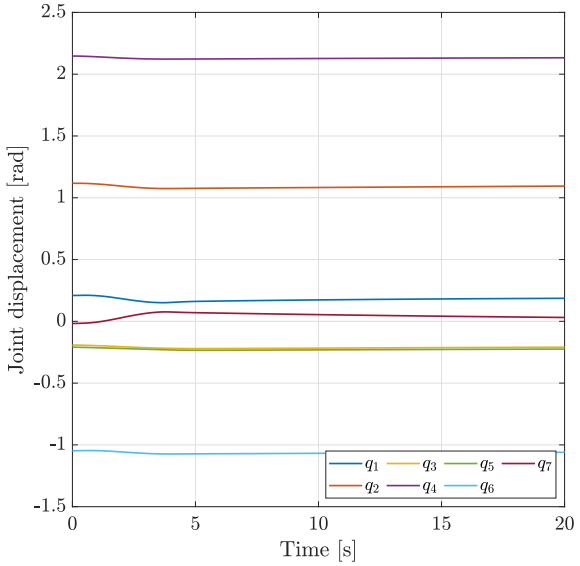

Fig. 17 Joint displacements - Scenario 1 Post-capture.

VII. Conclusion

This paper has presented the development and numerical validation of a coordinated control design for a spacecraft equipped with a robotic manipulator, with a focus on capturing and subsequently stabilizing a target object. Two relevant scenarios have been explored: a servicing mission of a large platform in GEO and a small satellite within a large constellation in LEO. Novel nonlinear laws embedding a quasi-time optimal feedback design have been developed,

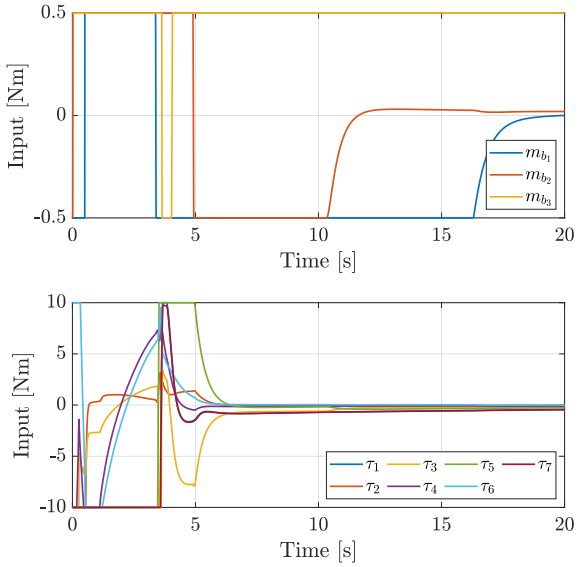

Fig. 18 Control actions - Scenario 1 Post-capture.

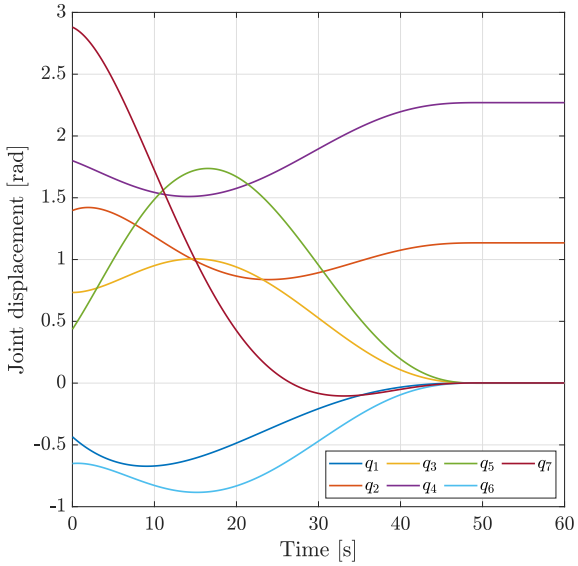

Fig. 19 Joint displacements - Scenario 2 Post-capture.

enabling effective handling of actuator saturations and ensuring high tracking control performance. An H_∞ synthesis procedure has been employed to systematically tune the gains of the control laws, accounting for fuel sloshing, and actuator and sensor dynamics. Thereafter, a robust stability routine has been adopted to verify performance of the tuned controller while managing parametric uncertainty and unmodeled dynamics. Moreover, a novel robust detumbling law, independent of the inertial parameters of the system, is proposed. This law is particularly attractive when the

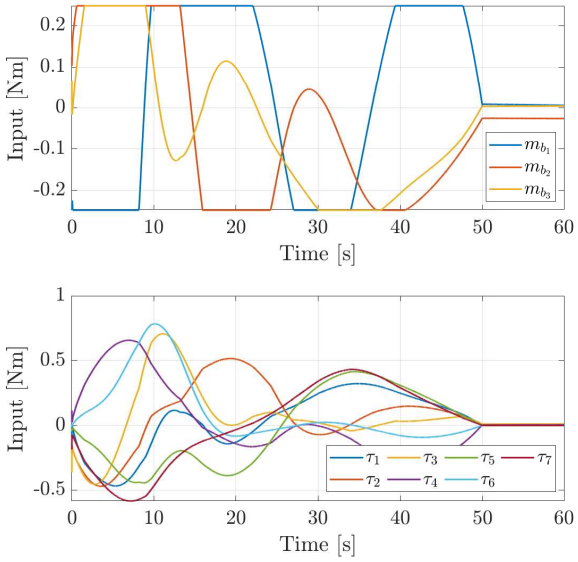

Fig. 20 Control actions - Scenario 2 Post-capture.

inertial parameters of the target are not known very accurately. Simulation results have validated the efficacy of the proposed control designs in the considered scenarios, demonstrating satisfactory performance even in the presence of challenging factors such as actuator saturation and sloshing effects. Future research directions may explore the possibility of integrating the guidance and control modules into a single unified block.

Acknowledgments

This work was in part supported by the European Space Agency (Contract NO. 4000132611/20/NL/CRS) in the context of the Open Invitations To Tender (ITT): ESA ITT 1-10250/20/NL/CRS.

References

[1] Estable, S., Pruvost, C., Ferreira, E., Telaar, J., Fruhnert, M., Imhof, C., Rybus, T., Peckover, G., Lucas, R., Ahmed, R., Oki, T., Wygachiewicz, M., Kicman, P., Lukasik, A., Santos, N., Milhano, T., Arroz, P., Biesbroek, R., and Wolahan, A., "Capturing and deorbiting Envisat with an Airbus Spacetug. Results from the ESA e.Deorbit consolidation phase study," *Journal of Space Safety Engineering*, Vol. 7, No. 1, 2020, pp. 52–66. https://doi.org/https://doi.org/10.1016/j.jsse.2020.01.003, URL https://www.sciencedirect.com/science/article/pii/S2468896720300070.

[2] Colmenarejo, P., Santos, N., Serra, P., Telaar, J., Strauch, H., De Stefano, M., Giordano, A. M., Mishra, H., Lampariello, R., Ott, C., Henry, D., and Visentin, G., "RESULTS OF THE COMRADE PROJECT: COMBINED CONTROL FOR ROBOTIC SPACECRAFT AND MANIPULATOR IN SERVICING MISSIONS: ACTIVE DEBRIS REMOVAL AND RE-FUELLING," 2021.

[3] Biesbroek, R., Aziz, S., Wolahan, A., Cipolla, S., Richard-Noca, M., and Piguet, L., "The ClearSpace-1 mission: ESA and ClearSpace team up to remove debris," 8th European Conference on Space Debris, ESA Space Debris Office, 2021.

[4] Pavanello, Z., Branz, F., Francesconi, A., Cenedese, A., Antonello, R., Basana, F., Iob, P., Vertuani, D., Massari, M., Colombo, C., et al., "Combined control and navigation approach to the robotic capture of space vehicles," *International Astronautical Congress: IAC Proceedings*, 2021, pp. 1–13.

[5] Basana, F., Pavanello, Z., Branz, F., Francesconi, A., Borelli, G., Invernizzi, D., Massari, M., Lovera, M., Nocerino, A., Opromolla, R., Huerts Garcia, I., and Pedro, S., "Satellite and robotic arm combined control for spacecraft close-proximity operations," *CEAS Space Journal*, 2025.

[6] Howell, E., "Two private satellites just docked in space in historic first for orbital servicing," https://www.space.com/private-satellites-docking-success-northrop-grumman-mev-1.html, 2020. Accessed: 27-03-2025.

[7] Invernizzi, D., Ghignoni, P., Ticozzi, L., Massari, M., Lovera, M., Simplicio, P., and Huertas Garcia, I., "Robust Control of Free-Flying Space Manipulator for Capturing Uncontrolled Tumbling Objects," *12th International Conference on Guidance, Navigation & Control Systems (GNC) and 9th International Conference on Astrodynamics Tools and Techniques (ICATT)*, 2023, pp. 1–15. https://doi.org/10.5270/esa-gnc-icatt-2023-146.

[8] Featherstone, R., *Rigid body dynamics algorithms*, Springer, New York, 2008. https://doi.org/https://doi.org/10.1007/978-1-4899-7560-7.

[9] Flores-Abad, A., Ma, O., Pham, K., and Ulrich, S., "A review of space robotics technologies for on-orbit servicing," *Progress in Aerospace Sciences*, Vol. 68, 2014, pp. 1–26. https://doi.org/https://doi.org/10.1016/j.paerosci.2014.03.002, URL https://www.sciencedirect.com/science/article/pii/S0376042114000347.

[10] Papadopoulos, E., Aghili, F., Ma, O., and Lampariello, R., "Robotic Manipulation and Capture in Space: A Survey," *Frontiers in Robotics and AI*, Vol. 8, 2021. https://doi.org/10.3389/frobt.2021.686723, URL https://www.frontiersin.org/journals/robotics-and-ai/articles/10.3389/frobt.2021.686723.

[11] Tsiotras, P., King-Smith, M., and Ticozzi, L., "Spacecraft-Mounted Robotics," *Annual Review of Control, Robotics, and Autonomous Systems*, Vol. 6, 2023, pp. 335–362. https://doi.org/https://doi.org/10.1146/annurev-control-062122-082114, URL https://www.annualreviews.org/content/journals/10.1146/annurev-control-062122-082114.

[12] Vafa, Z., and Dubowsky, S., "The Kinematics and Dynamics of Space Manipulators: The Virtual Manipulator Approach," *The International Journal of Robotics Research*, Vol. 9, No. 4, 1990, pp. 3–21. https://doi.org/10.1177/027836499000900401, URL https://doi.org/10.1177/027836499000900401.

[13] Papadopoulos, E., and Dubowsky, S., "Coordinated manipulator/spacecraft motion control for space robotic systems," *Proceedings. 1991 IEEE International Conference on Robotics and Automation*, 1991, pp. 1696–1701 vol.2. https://doi.org/10.1109/ROBOT.1991.131864.

[14] Aghili, F., "Coordination control of a free-flying manipulator and its base attitude to capture and detumble a noncooperative satellite," *2009 IEEE/RSJ International Conference on Intelligent Robots and Systems*, 2009, pp. 2365–2372. https://doi.org/10.1109/IROS.2009.5353968.

[15] Giordano, A. M., Dietrich, A., Ott, C., and Albu-Schäffer, A., "Coordination of thrusters, reaction wheels, and arm in orbital robots," *Robotics and Autonomous Systems*, Vol. 131, 2020, p. 103564. https://doi.org/https://doi.org/10.1016/j.robot.2020.103564, URL https://www.sciencedirect.com/science/article/pii/S0921889020304048.

[16] Kraïem, S., Rognant, M., Biannic, J.-M., and Brière, Y., "Dynamics and robust control of a space manipulator with flexible appendages for on-orbit servicing," *CEAS Space Journal*, Vol. 15, No. 5, 2023, pp. 681–700. https://doi.org/10.1007/s12567-022-00474-9, URL https://doi.org/10.1007/s12567-022-00474-9.

[17] Rodrigues, R., Preda, V., Sanfedino, F., and Alazard, D., "Modeling, robust control synthesis and worst-case analysis for an on-orbit servicing mission with large flexible spacecraft," *Aerospace Science and Technology*, Vol. 129, 2022, p. 107865. https://doi.org/https://doi.org/10.1016/j.ast.2022.107865, URL https://www.sciencedirect.com/science/article/pii/S1270963822005399.

[18] Huang, P., Wang, D., Meng, Z., Zhang, F., and Liu, Z., "Impact Dynamic Modeling and Adaptive Target Capturing Control for Tethered Space Robots With Uncertainties," *IEEE/ASME Transactions on Mechatronics*, Vol. 21, No. 5, 2016, pp. 2260–2271. https://doi.org/10.1109/TMECH.2016.2569466.

[19] Zhu, Y., Qiao, J., and Guo, L., "Adaptive Sliding Mode Disturbance Observer-Based Composite Control With Prescribed Performance of Space Manipulators for Target Capturing," *IEEE Transactions on Industrial Electronics*, Vol. 66, No. 3, 2019, pp. 1973–1983. https://doi.org/10.1109/TIE.2018.2838065.

[20] Forni, F., Galeani, S., and Zaccarian, L., "Globally stabilizing quasi time-optimal control of planar saturated linear systems," *2008 16th Mediterranean Conference on Control and Automation*, 2008, pp. 883–888. https://doi.org/10.1109/MED.2008.4602151.

[21] Apkarian, P., Gahinet, P., and Buhr, C., "Multi-model, multi-objective tuning of fixed-structure controllers," *2014 European Control Conference (ECC)*, IEEE, Strasbourg, France, 2014, pp. 856–861. https://doi.org/10.1109/ECC.2014.6862200.

[22] Luh, J. Y. S., Walker, M. W., and Paul, R. P. C., "On-Line Computational Scheme for Mechanical Manipulators," *Journal of Dynamic Systems, Measurement, and Control*, Vol. 102, No. 2, 1980, pp. 69–76. https://doi.org/10.1115/1.3149599, URL https://doi.org/10.1115/1.3149599.

[23] Yue, B.-Z., "Study on the Chaotic Dynamics in Attitude Maneuver of Liquid-Filled Flexible Spacecraft," *AIAA Journal*, Vol. 49, No. 10, 2011, pp. 2090–2099. https://doi.org/10.2514/1.J050144, URL https://doi.org/10.2514/1.J050144.

[24] Gasbarri, P., Sabatini, M., and Pisculli, A., "Dynamic modelling and stability parametric analysis of a flexible spacecraft with fuel slosh," *Acta Astronautica*, Vol. 127, 2016, pp. 141–159. https://doi.org/https://doi.org/10.1016/j.actaastro.2016.05.018, URL https://www.sciencedirect.com/science/article/pii/S0094576516300881.

[25] Pukniel, A., Kang, J.-Y., and Coverstone, V., "Determination of Acquisition Time and Wheel Control for Spacecraft Using a Momentum Transfer Technique," *AIAA Guidance, Navigation, and Control Conference*, American Institute of Aeronautics and Astronautics, Chicago, Illinois, 2009. https://doi.org/10.2514/6.2009-6110, URL https://arc.aiaa.org/doi/abs/10.2514/6.2009-6110.

[26] Bhat, S. P., and Bernstein, D. S., "A topological obstruction to continuous global stabilization of rotational motion and the unwinding phenomenon," *Systems & Control Letters*, Vol. 39, No. 1, 2000, pp. 63–70. https://doi.org/https://doi.org/10.1016/S0167-6911(99)00090-0, URL https://www.sciencedirect.com/science/article/pii/S0167691199000900.

[27] Bullo, F., and Murray, R. M., "Tracking for fully actuated mechanical systems: a geometric framework," *Automatica*, Vol. 35, No. 1, 1999, pp. 17–34. https://doi.org/https://doi.org/10.1016/S0005-1098(98)00119-8, URL https://www.sciencedirect.com/science/article/pii/S0005109898001198.

[28] Koditschek, D. E., "The Application of Total Energy as a Lyapunov Function for Mechanical Control Systems," *J. E. Marsden, P. S. Krishnaprasad and J. C. Simo (Eds) Dynamics and Control of Multi Body Systems*, Vol. 97, 1989, pp. 131–157. https://doi.org/10.1090/conm/097/1021035.

[29] Khalil, H., *Nonlinear Systems*, Pearson Education, Prentice Hall, 2002.

[30] Fernando, T., Chandiramani, J., Lee, T., and Gutierrez, H., "Robust adaptive geometric tracking controls on SO(3) with an application to the attitude dynamics of a quadrotor UAV," *IEEE Conference on Decision and Control and European Control Conference*, 2011, pp. 7380–7385. https://doi.org/10.1109/CDC.2011.6161306.

[31] Wang, J., Li, Y., and Zhao, X., "Inverse Kinematics and Control of a 7-DOF Redundant Manipulator Based on the Closed-Loop Algorithm," *International Journal of Advanced Robotic Systems*, Vol. 7, No. 4, 2010, p. 37. https://doi.org/10.5772/10495, URL https://doi.org/10.5772/10495.

[32] Caccavale, F., and Siciliano, B., "Quaternion-based kinematic control of redundant spacecraft/manipulator systems," *Proceedings 2001 ICRA. IEEE International Conference on Robotics and Automation (Cat. No.01CH37164)*, Vol. 1, IEEE, Seoul, South Korea, 2001, pp. 435–440. https://doi.org/10.1109/ROBOT.2001.932589.

[33] Yoshikawa, T., "Manipulability of Robotic Mechanisms," *The International Journal of Robotics Research*, Vol. 4, No. 2, 1985, pp. 3–9. https://doi.org/10.1177/027836498500400201, URL https://doi.org/10.1177/027836498500400201.

[34] Reed, B. B., Smith, R. C., Naasz, B. J., Pellegrino, J. F., and Bacon, C. E., *The Restore-L Servicing Mission*, 2016.

[35] Huang, S., Colombo, C., Gonzalo, J. L., Masserini, A., Nugnes, M., Vallini, L., and Petit, M., "Preliminary Mission Analysis of Active Debris Removal Service for Large Constellations," *International Astronautical Congress: IAC Proceedings*, 2020, pp. 1–6.

[36] Inaba, N., and Oda, M., "Autonomous satellite capture by a space robot: world first on-orbit experiment on a Japanese robot satellite ETS-VII," *Proceedings 2000 ICRA. Millennium Conference. IEEE International Conference on Robotics and Automation. Symposia Proceedings (Cat. No.00CH37065)*, Vol. 2, 2000, pp. 1169–1174 vol.2. https://doi.org/10.1109/ROBOT.2000.844757.

[37] Telaar, J., Estable, s., De Stefano, M., Rackl, W., Lampariello, R., Ankersen, F., and Gil-Fernandez, J., "Coupled Control of Chaser Platform and Robot Arm for the e.Deorbit Mission," *GNC 2017: 10th International ESA Conference on Guidance, Natigation & Control Systems*, 2017.